Journal of Catalysis 387 (2020) 47–61

Contents lists available at ScienceDirect

Journal of Catalysis

journal homepage: www.elsevier.com/locate/jcat

Zr–Ce-incorporated Ni/SBA-15 catalyst for high-temperature water gas shift reaction: Methane suppression by incorporated Zr and Ce

P. Hongmanorom[a], J. Ashok[a], S. Das[a], N. Dewangan[a], Z. Bian[a], G. Mitchell[b], S. Xi[c], A. Borgna[c], S. Kawi[a,*]

[a] Department of Chemical and Biomolecular Engineering, National University of Singapore, 4 Engineering Drive 4, Singapore 117585, Singapore
[b] Charles D. Davidson School of Chemical Engineering, Purdue University, 480 Stadium Mall Drive, West Lafayette, IN 47907, USA
[c] Institute of Chemical and Engineering Sciences, A*STAR (Agency for Science, Technology and Research), 1 Pesek Road, Jurong Island, Singapore 627833, Singapore

ARTICLE INFO

Article history:
Received 4 September 2019
Revised 29 October 2019
Accepted 13 November 2019
Available online 8 April 2020

Keywords:
Water-gas shift
Nickel catalyst
Ceria
Zirconia
Kinetic study

ABSTRACT

SBA-15 supports with incorporated Zr and/or Ce were synthesized using direct hydrothermal synthesis, followed by ammonia evaporation to prepare Ni–phyllosilicate-derived catalysts. The effect of zirconium and cerium ions present in the silica framework in catalyzing the high-temperature water–gas shift (WGS) reaction and circumventing the undesired methanation reaction was investigated over the temperature range from 250 to 500 °C. Diffuse-reflectance infrared Fourier transform spectroscopy revealed that surface hydroxyl species on silica were involved in promoting WGS activity for all catalysts. Furthermore, the presence of Zr and Ce in the silica framework could minimize the formation of Ni subcarbonyl species and enhance the adsorption of CO on Ni. At 375 °C, the Ni/Zr–Ce-SBA-15 catalyst achieved excellent catalytic activity in the WGS reaction in terms of turnover frequency (4.57 s^{-1}) and hydrogen formation rate (534 μmol H_2 $g^{-1}s^{-1}$). A dual-site carboxyl mechanism was proposed to be the plausible pathway over the Ni/Zr–Ce-SBA-15 catalyst.

1. Introduction

The water-gas shift (WGS) reaction via the reaction of steam with carbonaceous feedstocks (either from fossil fuel or renewable sources) is one of the essential steps involved in industrial processes such as Fischer–Tropsch synthesis and hydrogen production [1–3]. Specifically, the WGS reaction plays a key role in enriching hydrogen (H_2) and removing carbon monoxide (CO) from reforming syngas, which is a mixture consisting primarily of H_2 and CO [3,4]:

$$CO + H_2O \rightarrow CO_2 + H_2 \; (\Delta H_{298} = -41.2 \text{ kJ/mol}). \tag{1}$$

Ni-based catalysts have been extensively studied for reforming of hydrocarbons [5–8] and the WGS reaction [9–12] due to their low cost and high catalytic activity, especially at high temperatures (350–450 °C). However, their application to the WGS reaction in the industry has been retarded because of the undesirable methanation side reaction, which reduces the H_2 yield [13]. Several approaches have been applied to suppress methanation in the high-temperature WGS reaction, such as the addition of alkali and alkaline metals as promoters [9,14–17], alloy formation of Ni with a second metal, or the bimetallic catalyst formulations [18,19], and core–shell-like catalyst formulations [20]. Recently, our research group has reported Ni-embedded Ni–phyllosilicate (Ni/SiO_{2p}) catalysts for the high-temperature WGS reaction and revealed the role of surface hydroxyl species (—OH) in promoting WGS activity and methane suppression [10]. Besides the SiO_2 support, Ni metal can also react with mesoporous silica, such as SBA-15 [21] and MCM-41 [22], during catalyst preparation method and generate Ni–phyllosilicate mesoporous silica composites. Ni-based SBA-15 catalysts have been also widely used in steam reforming [6,23] and dry reforming reactions [24–27] because of their high BET surface areas, large pore volumes, and highly ordered pore structures with narrow pore size distributions in the range of 2–50 nm. SBA-15 could provide not only plenty of catalytic active sites but also a confinement effect, preventing metal nanoparticles from sintering and alleviating carbon deposition.

In addition to OH species present in the phyllosilicate structure, surface OH groups can also be produced via water dissociation or the reaction of water with oxygen vacancies of metal oxides such as CeO_2, ZrO_2, TiO_2, and La_2O_3 [28–30]. These partially reducible materials with large oxygen storage capacity are common supports used in WGS reaction [31,32]. A number of studies have shown that the addition of ZrO_2 to CeO_2 also improves oxygen storage capacity, redox properties, and thermal resistance [33–35]. Over the past decade, incorporation of heteroatoms such as Ce and Zr

---

[*] Corresponding author.
E-mail address: chekawis@nus.edu.sg (S. Kawi).

https://doi.org/10.1016/j.jcat.2019.11.042
0021-9517/

into ordered mesoporous silica has been developed to promote the mobility of surface oxygen species over catalyst surfaces. Wu et al. reported an increase of catalytic activity in CO_2 reforming of ethanol due to the presence of Ce in Rh/SBA-15 crystalline lattice, which enhances surface oxygen vacancies [24]. Similarly, Vargas et al. reported that the cerium ions in the MCM-41 framework might promote oxygen motion and reducibility in the Rh—O bond [36]. Thus, Rh/Ce-MCM-41 catalysts exhibited superior catalytic performance in ethanol steam reforming compared with that of the Rh/MCM-41 catalyst. Furthermore, the addition of Zr or Ce can prevent hydrolysis of Si—O—Si bonds, which in turn improves hydrothermal stability of silica [37,38].

Herein, Ce and/or Zr incorporated mesoporous SBA-15 supports were synthesized via direct hydrothermal synthesis. Ni–phyllosilicate-derived catalysts were then prepared using ammonia evaporation and used to investigate the roles of surface hydroxyls in catalyzing high-temperature WGS reaction and the presence of Zr and Ce in suppressing methane formation. *In situ* DRIFTS, mass spectroscopy, and kinetic studies were also performed to elucidate the possible reaction mechanism for Zr–Ce-incorporated Ni/SBA-15 catalyst in the high-temperature WGS reaction.

2. Experimental

2.1. Catalyst synthesis

SBA-15 support was synthesized according to the method reported by Zhao et al. [39]. Ce-SBA-15, Zr-SBA-15, and Zr–Ce-SBA-15 catalyst supports were also prepared by direct hydrothermal synthesis method using amphiphilic P123 triblock copolymer (EO20PO70EO20, molecular weight = 5800, Sigma-Aldrich, CAS: 9003-11-6) as the template and tetraethyl orthosilicate (TEOS, Sigma-Aldrich, CAS: 78-10-4) as the silica source. First, 1.0 g of Pluronic P123 was dissolved in 40.0 g of 2 M HCl solution under stirring until complete dissolution of polymer was achieved. Then 2.1 g of TEOS was added to the solution dropwise. Next, $Ce(NO_3)_3\cdot 6H_2O$ (Sigma-Aldrich, CAS: 10294-41-4) and/or $ZrOCl_2\cdot 8H_2O$ (Sigma-Aldrich, CAS: 13520-92-8) was added into this solution under stirring. The mixed solution was continuously stirred for 24 h at 40 °C and finally crystallized in a Teflon-lined stainless steel autoclave at 100 °C for 24 h. The precipitate was filtered, washed with DI water, and dried overnight at 80 °C. The organic template was removed from the porous structure by calcination at 550 °C for 6 h at a heating rate of 1.5 °C/min. The products were obtained and designated as Ce-SBA-15 (molar ratio of Ce/Si = 0.1), Zr-SBA-15 (molar ratio of Zr/Si = 0.1), and Zr–Ce-SBA-15 (molar ratio of Zr/Si = 0.05 and Ce/Si = 0.05).

After the synthesis of support materials, 10 wt% Ni-loaded catalysts were prepared by the ammonia evaporation method. A 25% aqueous ammonia solution (6 ml) was dissolved in 44 ml of deionized water. Then,1.1 g of $Ni(NO_3)_2\cdot 6H_2O$ (Sigma-Aldrich, 99.99%, CAS: 13478-00-7) was added to the aqueous ammonia solution and stirred for 10 min. Next, 2.0 g of support materials was added to the mixture and stirred at 80 °C. After 4 h, the obtained product was filtered, washed with deionized water, and dried overnight at 120 °C. Finally, it was calcined for 4 h at 400 °C with a heating rate of 1.5 °C /min to obtain the catalyst.

2.2. Catalyst characterization

2.2.1. BET surface area

Micromeritics ASAP-2020 adsorption apparatus was used to determine the specific surface area, pore volume, and pore size of the support materials and reduced catalysts. They were measured by N_2 physical adsorption at −196 °C by the Brunauer–Emmett–Teller (BET) method. Prior to analysis, the volatile species adsorbed on the catalyst surface were eliminated by heating the catalyst under vacuum for 4 h at 350 °C.

2.2.2. X-ray diffraction

X-ray diffraction (XRD) was employed to characterize the crystallinity of the catalysts. The XRD analyses were performed using a Shimadzu XRD-6000 X-ray diffractometer with Cu$K\alpha$ X-ray source radiation and operated at 40 kV and 30 mA with the following slit parameters: divergence slit of 1°, scattering slit of 1°, and receiving slit of 0.3 mm. The step size was scanned at 2°/min while the 2θ range was measured from 20° to 80°. The average Ni^0 crystal size was calculated from the (1 1 1) plane of Ni at around $2\theta = 44.6°$ in XRD patterns using the Debye–Scherrer equation, $D = K\lambda/\beta\cos\theta$, where D is crystallite size (nm); K is crystallite-shape factor, which is 0.9; λ is the X-ray wavelength for Cu$K\alpha$, which is 0.15418 nm; β is half-height width; and θ is the Bragg angle.

2.2.3. H_2 temperature-programmed reduction

Temperature-programmed reduction (TPR) was performed for fresh catalysts using a Thermo Scientific TPDRO-1100 series system equipped with a thermal conductivity detector. Prior to the TPR analysis, about 50 mg of catalyst was loaded in an isothermal zone and outgassed in 30 ml/min He gas at a heating rate of 10 °C / min to 300 °C to remove impurities and physically adsorbed water. After the sample was cooled to room temperature, 30 ml/min of 5% H_2/N_2 gas was flowed while the temperature was increased from 50 to 950 °C at a heating rate of 10 °C/min.

2.2.4. N_2O pulse titration

The surface Ni metal content was measured using a Thermo Scientific TPDRO-1100 series system. The first H_2 TPR was performed at 700 °C for 1 h to reduce the catalyst, followed by cooling to 80 °C under N_2 gas. Then several pulses of purified N_2O gas were injected until saturation was reached, in which the constant eluted peak area of consecutive pulses was observed. After cooling to room temperature, the second H_2 TPR was conducted at up to 700 °C. It was assumed that one molecule of N_2O is stoichiometrically adsorbed on one atom of Ni on the catalyst surface. Thus, the number of surface Ni atoms was determined from the amount of adsorbed N_2O.

2.2.5. Transmission electron microscopy

The morphology and metal particle sizes of the catalysts were characterized using a JEOL JEM-2100F high-resolution transmission electron microscopy (HRTEM) system. Prior to the analysis, the catalyst was reduced at 700 °C under H_2 for 1 h. The sample was then dispersed in a volatile liquid, ethanol, and sonicated for 15 min. The suspension was dropped onto perforated copper grids and dried in air. The high-angle annular dark-field scanning transmission electron microscopy (HAADF-STEM) was also performed, equipped with an EDX detector.

2.2.6. X-ray photoelectron spectroscopy

Surface analysis of the reduced catalysts was performed by X-ray photoelectron spectroscopy (XPS) using a KRATOS AXIS Ultra spectrometer equipped with a monochromatic Al$K\alpha$ X-ray source ($h\nu$ = 1486.71 eV). Prior to the analysis, the catalyst was reduced under H_2 for 1 h at 700 °C. The sample was then placed on the standard sample stub. The obtained binding energies were calibrated to the position of C1S (284.50 eV) as the reference.

2.2.7. X-ray absorption spectroscopy

Ni K-edge X-ray absorption spectroscopy (XAS) was carried out in transmission mode at the XAFCA beamline of the Singapore

Synchrotron Light Source. Boron nitride was used to dilute appropriate amounts of sample prior to disk-shaped palletization.

2.2.8. Diffuse reflectance UV–visible

Diffuse reflectance UV–visible (DRUV–vis) spectra were recorded by a Shimadzu UV-3600 spectrophotometer. The powder samples were loaded into a plate cell where barium sulfate ($BaSO_4$) was used as a reference material. Then the spectra were collected in the range of 190–600 nm.

2.2.9. Diffuse reflectance infrared Fourier transform spectroscopy

In situ CO diffuse reflectance infrared Fourier transform spectroscopy (DRIFTS) studies were conducted using a Bruker FTIR Vertex 70 spectrometer equipped with a Harrick Praying Mantis DRIFTS cell connected to a controlled gas system. Due to the high reduction temperature of 700 °C, the reduced catalyst was re-reduced in the reaction chamber at 550 °C for 30 min under H_2 gas prior to the analysis. During cooling to 50 °C, He gas was flowed to purge the remaining H_2 gas for 20 min, followed by background spectra collection. Subsequently, 5% CO in He or 5% CO and 25% H_2O in He were introduced into the reaction chamber while heating up to 500 °C with 50 °C intervals. At each temperature, the spectra were scanned 100 times at a resolution of 4 cm^{-1} and the DRIFTS data were collected at 1-, 5-, and 15-min intervals.

2.2.10. CO temperature-programmed reduction–mass spectroscopy

A fixed-bed reactor system coupled with a Shimadzu gas chromatograph mass spectrometer (GCMS-QP2010) was employed to conduct CO temperature-programmed reduction (TPR) experiments. Catalyst (50 mg) was first reduced for 1 h under H_2 gas at 700 °C and then cooled to room temperature under flushed He gas. For the analysis, 5% CO in He gas mixture with a total flow rate of 60 ml/min was flowed through the reactor, which was heated to 900 °C at a heating rate of 10 °C /min. The effluent gas was continuously monitored and measured using mass spectroscopy (MS).

2.3. Catalytic activity measurement

The WGS activity was evaluated in a fixed-bed quartz reactor with an inner diameter of 4 mm and a length of 400 mm. Prior to the reaction, the catalyst was reduced for 1 h in 20 ml/min H_2 at 700 °C, followed by cooling to the desired reaction temperature (250 °C) under He gas. Water was vaporized at 150 °C with a preheater to generate steam, which was further delivered to mix with reactant gases by a HPLC pump. The reactant gases consisted of 5 mol.% CO, 25 mol.% H_2O, and the balance He to make up a total flow rate of 50 ml/min with a GHSV of 40,000 h^{-1}, unless otherwise specified. The unreacted water in the effluent was condensed when passing through a cold trap set at 5 °C, while the remaining non-condensable product gases were analyzed online using an HPGC equipped with a Hayesep D column. The data collection was conducted when the steady state had been reached.

The CO conversion was calculated according to the equation

$$X_{CO} = \frac{[CO]_{in} - [CO]_{out}}{[CO]_{in}} \times 100\%. \quad (2)$$

The CH_4 and H_2 yield (%) were calculated according to the equation

$$\%\ CH_4\ (H_2)\ \text{yield} = \frac{[CH_4]_{out}([H_2]_{out})}{[CO_2]_{out} + [H_2]_{out} + [CH_4]_{out}} \times 100\%. \quad (3)$$

The turnover frequency (TOF) and the reaction rates were determined by testing the catalytic activity with diluted catalysts (diluted with quartz SiO_2 powder) and a total flow rate of 100 ml/min to maintain the CO conversion below 15%. The TOF and H_2 rate were calculated as follows:

$$\text{TOF}\ (s^{-1}) = \frac{\text{mol of CO converted}}{\text{mol of surface Ni atoms x time (s)}}, \quad (4)$$

$$H_2\ \text{rate} = \frac{\text{mol of } H_2 \text{ produced}}{\text{mass of catalsyt (g) x time (s)}}. \quad (5)$$

The kinetic measurements were conducted using Ni/Zr–Ce-SBA-15 catalyst diluted with quartz SiO_2 powder to keep the total CO conversion below 15%. The study was taken over the gas composition range of 2.5–12.5% CO, 10–55% H_2O, 5–25% CO_2, 5–20% H_2, and balance He. The apparent reaction order was also measured under these conditions at 375 °C. All measurements were performed under atmospheric pressure and after reaching steady state. The rate of reaction was calculated using the following formula:

$$\text{Rate}\ (r) = \frac{\text{mol of CO converted}}{\text{metal surface area } (m^2) \text{ x time (s)}}. \quad (6)$$

3. Results and discussion

3.1. Textural properties of catalyst supports and catalysts

Fig. 1 illustrates the N_2 adsorption–desorption isotherms of the catalysts. The profile of Ni/SBA-15 displays a type IV isotherm, according to the IUPAC classification, along with an H1-type hysteresis loop in the range P/P_0 = 0.65–0.9, which is characteristic of mesoporous materials with one-dimensional cylindrical channels. When Zr and/or Ce ions were inserted into the SBA-15 framework, the shape of the type IV isotherm was still maintained. Besides, the inflection step was reduced, indicating a slight decrease in ordered mesoporosity. The physicochemical properties of SBA-15 supports with incorporated Ce and/or Zr and their respective supported Ni catalysts are summarized in Table 1. As compared with pure SBA-15, decreases in BET surface area, total pore volume, and average pore diameter of Ce-SBA-15, Zr-SBA-15, and Zr–Ce-SBA-15 supports were observed. A possible explanation for these reductions might be that some tiny and well-dispersed Zr and/or Ce species deposited at the inner pore walls and/or external surface areas. After loading of Ni, their BET surface area and total pore volume were subsequently reduced, suggesting

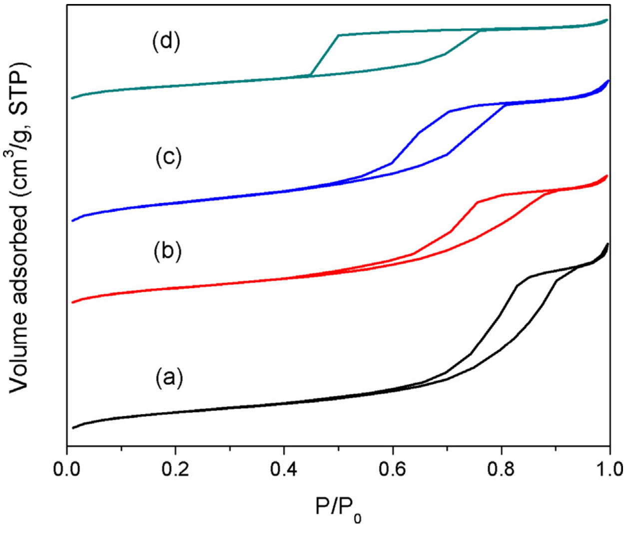

Fig. 1. N_2 adsorption–desorption isotherms of reduced (a) Ni/SBA-15, (b) Ni/Ce-SBA-15, (c) Ni/Zr-SBA-15, and (d) Ni/Zr–Ce-SBA-15 catalysts.

Table 1
Physicochemical properties of Ni/SBA-15 catalysts with incorporated Ce and/or Zr.

Catalyst	BET surface area (m^2/g)	Total pore volume (cm^3/g)	Average Pore diameter (nm)	Ni crystal size (nm) [a]	Ni particle size (nm) [b]	Ni metal surface area (m^2/g_{cat}) [c]
SBA-15	899	1.3	5.6	–	–	–
Ce-SBA-15	884	1.2	5.3	–	–	–
Zr-SBA-15	817	1.2	5.4	–	–	–
Zr–Ce-SBA-15	776	0.9	4.7	–	–	–
Ni/SBA-15	377	1.0	10.5	4.8	4.2	5.8
Ni/Ce-SBA-15	355	0.7	7.8	4.6	4.1	5.4
Ni/Zr-SBA-15	337	0.8	7.2	4.5	4.1	4.7
Ni/Zr–Ce-SBA-15	324	0.6	5.8	4.6	4.1	4.6

[a] Ni crystal size was determined from the (1 1 1) plane of Ni in XRD patterns using the Debye–Scherrer equation.
[b] Average Ni particle size was measured from 100 particles observed in TEM images.
[c] Metal surface area was determined by N_2O pulse titration.

the embedding of Ni particles in the SBA-15 pores, while their average pore diameters were increased due to collapse of smaller pores.

3.2. H_2 temperature-programmed reduction

As shown in Fig. 2, the H_2 TPR technique was employed to investigate the reduction behavior of Ni/SBA-15, Ni/Zr-SBA-15, Ni/Ce-SBA-15, and Ni/Zr–Ce-SBA-15 catalysts. Typically, the reduction peak at around 270–300 °C is ascribed to the presence of bulk NiO particles converted to Ni^0 species [40]. The peak before 500 °C is assigned to the reduction of NiO species, either located on the external surface or immobilized within the channels of mesoporous SBA-15. The Ni/SBA-15 catalyst exhibited a main peak at high temperature around 775 °C, which was likely to be the reduction of Ni^{2+} species strongly interacting with silica, specifically nickel–phyllosilicate species [41]. This reduction peak shifted toward lower temperature from 775 to 735 °C with the presence of Zr in the silica framework, indicating the role of Zr incorporation in promoting the reducibility of Ni species. In case of Ni/Ce-SBA-15 catalyst, the downward peak shift was greater than in the Ni/Zr-SBA-15 catalyst (centered at 645 °C) due to the fact that ceria possesses higher mobility and surface active oxygen than zirconia [38]. The peak became broader and shifted to even lower temperature for Ni/Zr–Ce-SBA-15 catalyst, showing a center at around 570 °C. Overall, no obvious peak was detected under 400 °C, suggesting intimate contact between metal and support.

3.3. X-ray diffraction of calcined and reduced catalysts

In Fig. 3, the presence of Ni-containing phyllosilicate was detected by XRD pattern. All calcined catalysts exhibited three weak diffraction peaks at 2θ = 33.7°, 36.7°, and 60.9°, corresponding to the (2 0 0), (2 0 2), and (0 6 0) planes of Ni–phyllosilicate, respectively. The diffraction peaks at 37.2° and 43.2°, which are attributed to the (1 1 1) and (2 0 0) reflections of NiO, were not present in the XRD pattern, demonstrating high dispersion of NiO particles in SBA-15 based support [42,43].

Fig. 4 shows the XRD patterns of catalysts reduced at 700 °C for 1 h. A broad peak was observed at around 2θ = 44.6° corresponding to the presence of the Ni(1 1 1) crystalline phase, indicating very small Ni particles with high dispersion for all catalysts. No significant change in the XRD profiles was observed with the incorporation of Zr and Ce into the framework of mesoporous silica. The average crystallite sizes of Ni derived using the Debye–Scherrer equation are shown in Table 1. The result was further compared with the average Ni particle size obtained from TEM images.

3.4. Transmission electron microscopy

The surface morphologies of calcined and reduced catalysts are displayed in Figs. 5 and 6, respectively. In Fig. 5, scanning transmission electron microscopy high-angle annular dark-field (STEM-HAADF) presents the characteristic fibrous microstructures of Ni-phyllosilicate in calcined Ni/Zr–Ce-SBA-15 catalyst. With the

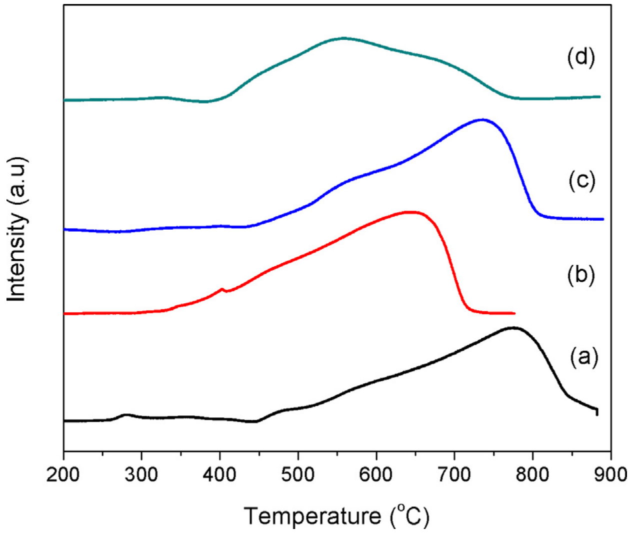

Fig. 2. TPR profiles of calcined (a) Ni/SBA-15, (b) Ni/Ce-SBA-15, (c) Ni/Zr-SBA-15, and (d) Ni/Zr–Ce-SBA-15 catalysts.

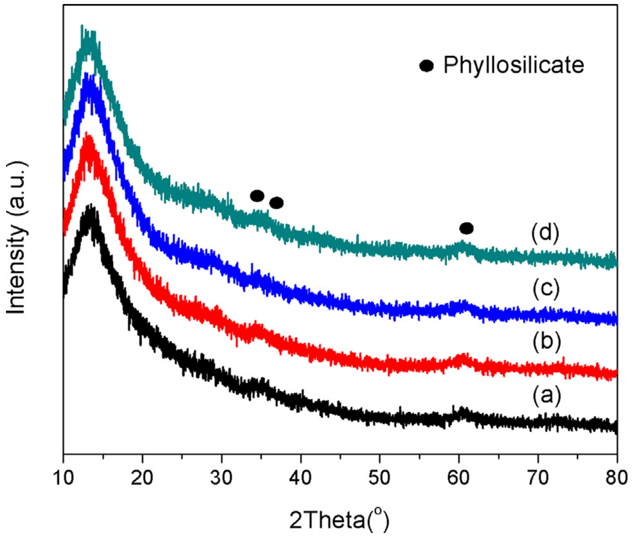

Fig. 3. XRD patterns of calcined (a) Ni/SBA-15, (b) Ni/Ce-SBA-15, (c) Ni/Zr-SBA-15, and (d) Ni/Zr–Ce-SBA-15 catalysts.

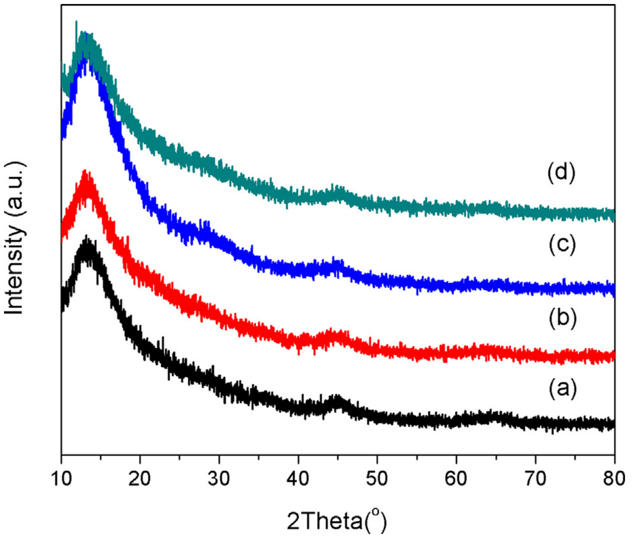

Fig. 4. XRD patterns of reduced (a) Ni/SBA-15, (b) Ni/Ce-SBA-15, (c) Ni/Zr-SBA-15, and (d) Ni/Zr–Ce-SBA-15 catalysts.

incorporation of Ce and/or Zr species into the silica framework, short mesochannels were observed. It has been reported in the literature that the presence of Zr and Ce ions is likely to accelerate silicate condensation around the micelles, which in turn produces the short-channel mesoporous structure [44]. EDX analysis qualitatively suggested the homogeneous distribution of Ni, Zr, and Ce within calcined SBA-15 catalyst, although some small fraction of Zr and Ce species also dispersed outside the channels. In addition, the fibrous structure of Ni–phyllosilicate was found to preferably form at the edge position and on the external surface rather than aligning inside the channels [45].

As shown in Fig. 6, reduced catalysts clearly possessed a well-ordered hexagonal array of channels. The alignment of the pores was mostly perpendicular to the electron beam direction, exhibiting a regular interpore distance. It was also found that Ni particles were well dispersed and uniformly incorporated into the ordered mesoporous channels of SBA-15 in all catalysts, with average particle sizes of around 4 nm, which were similar to crystal sizes calculated by the Scherrer equation (Table 1). As reported in the literature, SBA-15 supported nickel catalyst prepared by ammonia evaporation exhibited a narrow particle size distribution with a maximum centered at approximately 4 nm.

3.5. X-ray photoelectron spectroscopy measurements

X-ray photoelectron spectroscopy (XPS) was utilized to obtain surface information in reduced catalysts. The Ni2$p_{3/2}$ XPS spectra of the reduced catalysts are shown in Fig. 7, exhibiting two kinds of Ni2$p_{3/2}$ binding energies (BEs). The first peak, at around 852.7 eV (BE), is attributed to the Ni^0 species, and the second peak, at 855.7 eV, with a shake-up satellite peak at 861.3 eV, is assigned to the Ni^{2+} species [46,47]. As observed from the TPR profile, not all reducible species could be reduced at 700 °C, and thus the unreduced Ni species could contribute to the presence of Ni^{2+} species in the XPS spectra. The presence of Ni^{2+} species in the phyllosilicate structure over the catalysts reduced at 700 °C was consistent with earlier observations by Ashok et al. [10]. It has also been reported that the interaction between Ni metals and CeO_2 can cause the existence of Ni^{2+} species [48]. A slight shift toward lower value of Ni2$p_{3/2}$ BEs was observed from 852.7 to 852.5 eV for Ce- and/or Zr-incorporated Ni/SBA-15 catalysts. This chemical shift may be indicative of interaction between Ni and Ce and/or Zr. Also, the addition of Ce and Zr may increase the electron density of Ni on the catalyst surface [14]. As presented in Table 2, the relative concentration of Ni^0 to Ni^{2+} was determined to be 0.18, 0.27, 0.19, and 0.29 for Ni/SBA-15, Ni/Ce-SBA-15, Ni/Zr-SBA-15, and Ni/Zr–Ce-SBA-15 catalysts, respectively. A higher concentration of Ni^0 relative to Ni^{2+} suggested that the presence of Ce and/or Zr may facilitate the reducibility of Ni species. Furthermore, the surface Ni content for all catalysts was similar, approximately 2.2–2.5%. Some nickel species embedded in the silica matrix might be undetectable due to the limitation of XPS source rays' penetration ability during the analysis. The surface Si concentration decreased

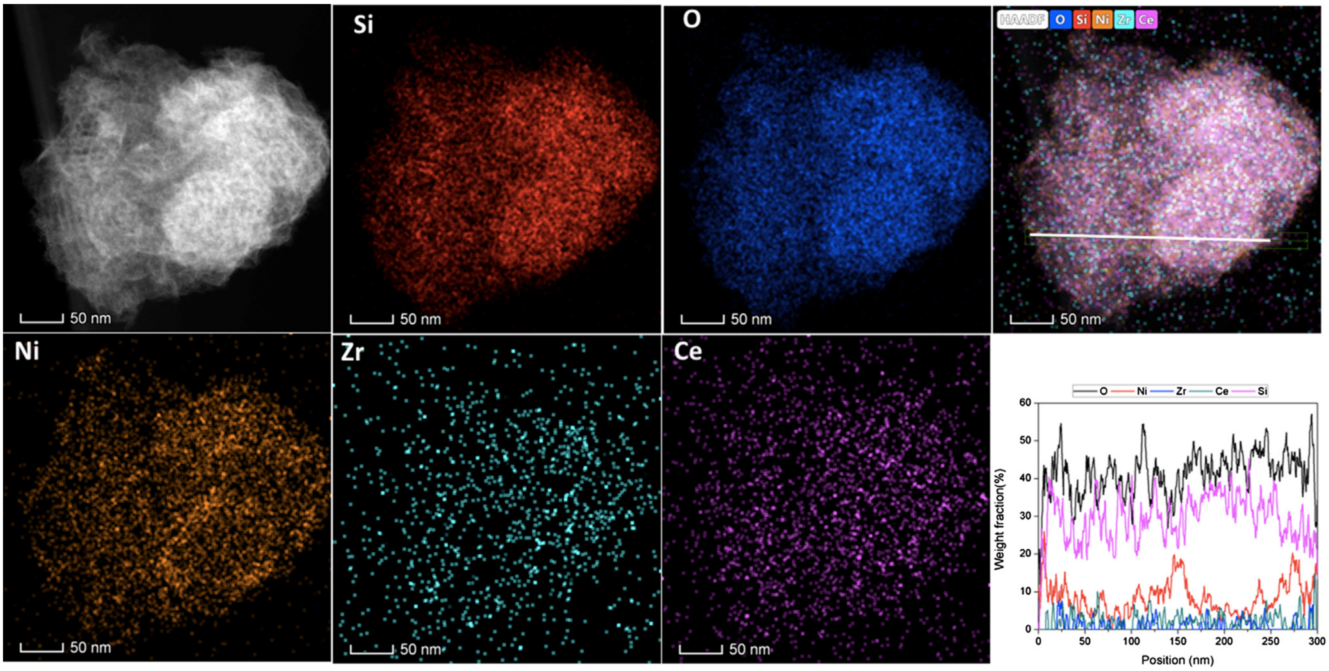

Fig. 5. STEM-HADDF image and EDS mapping of calcined Ni/Zr–Ce-SBA-15 catalyst.

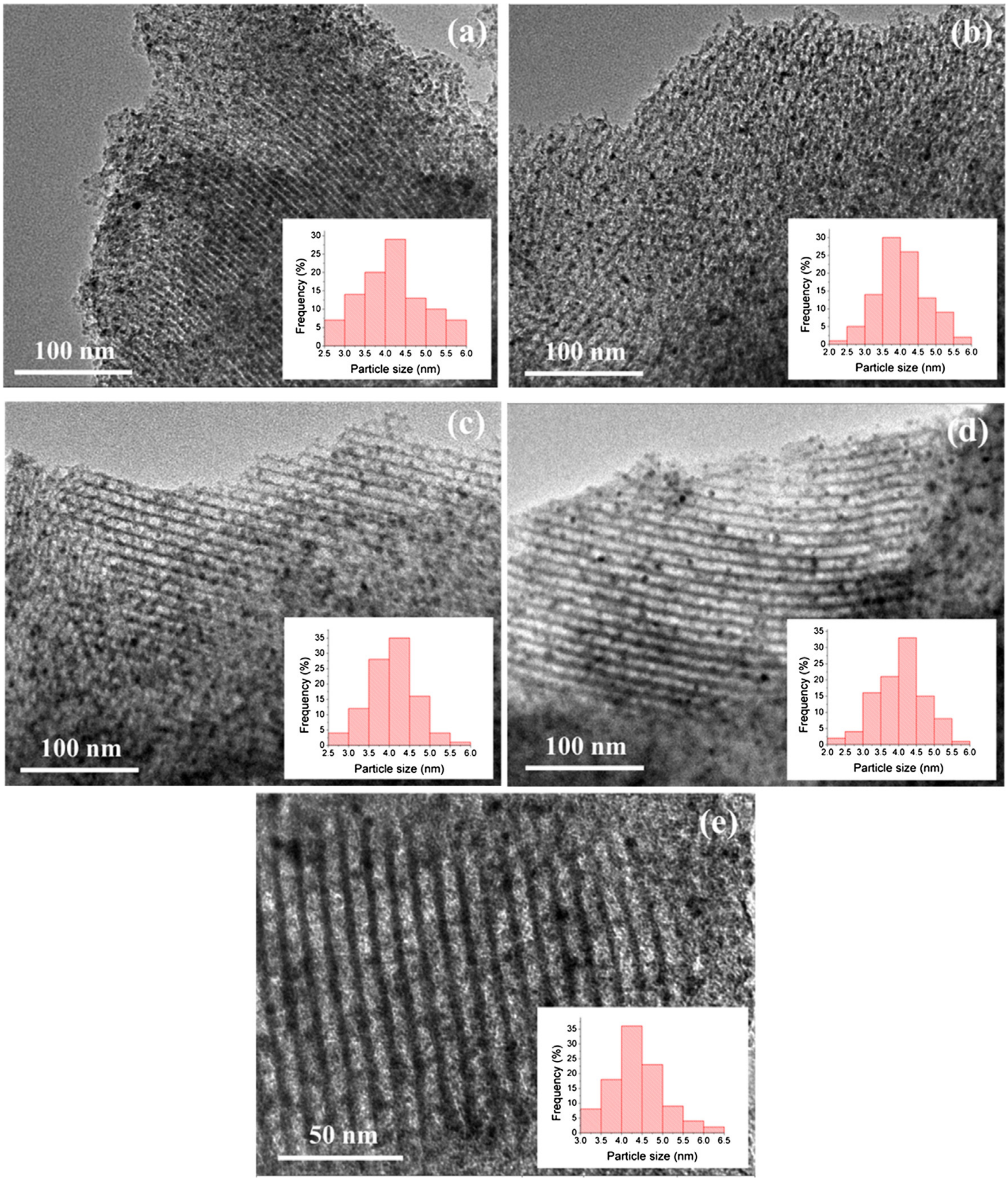

Fig. 6. TEM images for (a) reduced Ni/SBA-15, (b) reduced Ni/Ce-SBA-15, (c) reduced Ni/Zr-SBA-15, (d) reduced Ni/Zr–Ce-SBA-15, and (e) spent Ni/Zr–Ce-SBA-15 after 70 h.

slightly with the addition of Zr and/or Ce, possibly indicating their incorporation into the silica framework and/or dispersion on the external surface of the catalyst.

3.6. X-ray absorption spectroscopy analysis

The elemental oxidation states of the reduced catalysts, Ni/SBA-15 and Ni/Zr–Ce-SBA-15, were also probed by XANES and compared with the spectra of Ni foil (Ni^0) and NiO (Ni^{2+}) as a reference. The XANES spectra of Ni^{2+} in the NiO phase presented a pre-edge peak and white line at 8350.2 eV, whereas those of metallic Ni^0 showed a weaker pre-edge peak with a weaker white line (Fig. 8a) [49,50]. In Fig. 8b, both reduced catalysts exhibited a small white line, indicating that Ni–phyllosilicate was not completely reduced to Ni^0 at 700 °C. Rodriguez-Gomez et al. [51] reported the complete reduction of phyllosilicate-derived Ni/SBA-15 catalyst prepared via deposition–precipitation method above 750 °C. However, Ni/Zr–Ce-SBA-15 catalyst showed a weaker pre-edge peak, possibly due to easier reduction to the metallic state. These results were in agreement with the H_2 TPR and XPS results presented above.

3.7. Diffuse reflectance UV–visible

DRUV–vis was used to identify the chemical environment and coordination structure of metal ions in the framework and/or extra-framework of silica materials. As reported in the literature [52], the NiO spectrum typically exhibited a broad band in the range 250–350 nm with high intensity and other weak adsorption bands at 381, 411, and 550 nm. These absorption bands indicated

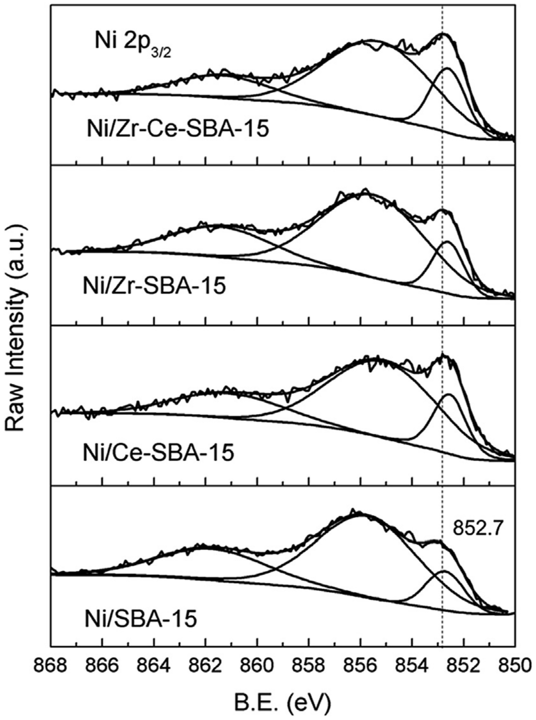

Fig. 7. XPS spectra for the Ni2$p_{3/2}$ of the reduced catalysts.

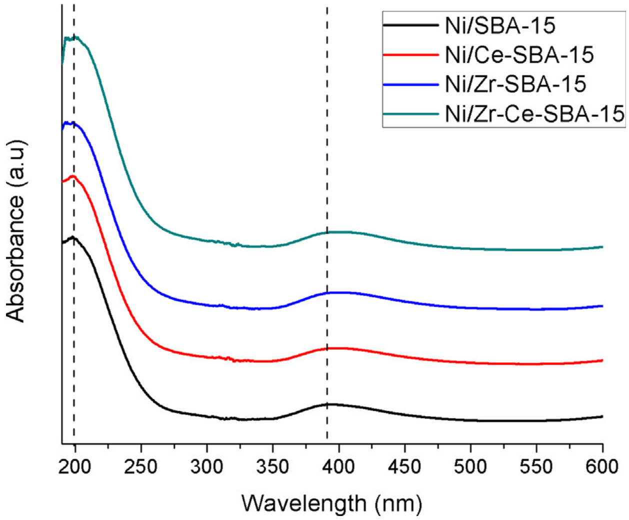

Fig. 9. UV–vis spectra of Ni/SBA-15, Ni/Ce-SBA-15, Ni/Zr-SBA-15, and Ni/Zr–Ce-SBA-15 catalysts.

the presence of Ni^{2+} ions in an octahedral coordination environment. These NiO absorption bands were not observed for all catalysts in Fig. 9, except a weak band covering 350–450 nm. Additionally, one narrow band at lower wavelength (around 197 nm) was observed for all catalysts. These results suggested the existence of Ni-containing phyllosilicates in tetrahedral coordination [22,52]. The UV–vis spectra of Ni/Ce-SBA-15 and Ni/Zr–Ce-SBA-15 catalysts did not resemble those of bulk CeO_2, which exhibited two bands at about 271 and 347 nm corresponding to an $O^{2-} \rightarrow Ce^{4+}$ ligand-to-metal charge transfer (LMCT) and interband transitions, respectively [53]. Likewise, the absorption band at about 240 nm, which is ascribed to the O → Zr(IV) LMCT

Table 2
Surface composition derived from XPS.

Catalyst	Surface elemental composition (wt.%)[a]					Nickel ratio $[Ni^0]/[Ni^{2+}]$
	Ni	Si	O	Ce	Zr	
Ni/SBA-15	2.3	33.2	64.5	0	0	0.18
Ni/Ce-SBA-15	2.5	32.6	64.3	0.6	0	0.27
Ni/Zr-SBA-15	2.2	32.7	64.5	0	0.6	0.19
Ni/Zr–Ce-SBA-15	2.4	32.0	64.7	0.5	0.4	0.29

[a] Surface elemental composition was calculated using CasaXPS software with the equation $A\% = \frac{\frac{Area_A}{RSF_A}}{\frac{Area_A}{RSF_A}+\frac{Area_B}{RSF_B}+\frac{Area_C}{RSF_C}+\frac{Area_D}{RSF_D}+\frac{Area_E}{RSF_E}}$, where relative sensitivity factors (RSF) were used to scale the measured peak areas.

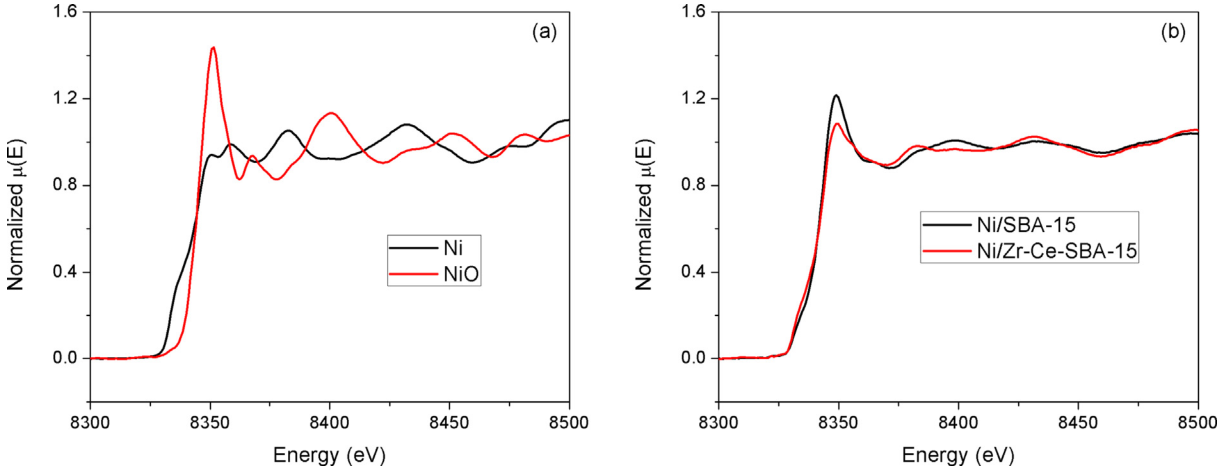

Fig. 8. Ni *K*-edge XANES spectra for (a) Ni and NiO and (b) reduced Ni/SBA-15 and Ni/Zr–Ce-SBA-15 catalysts.

transition in ZrO_2, was not detected for Ni/Zr-SBA-15 and Ni/Zr–Ce-SBA-15 catalysts [54]. The absence of these bands in UV–vis spectra of Zr- and/or Ce-incorporated Ni/SBA-15 catalysts indicated the absence of bulk CeO_2 and ZrO_2 as well as implying the formation of Zr and Ce in different species, specifically isolated Zr and Ce species in the silica framework or small CeO_2 and ZrO_2 clusters on the pore wall. For Ni/Zr-SBA-15 and Ni/Zr–Ce-SBA-15 catalysts, an additional narrow band at 194 nm, which is attributed to LMCT transition of O → Zr(IV) centers of well-dispersed zirconium species inside the silica matrix, was also observed [55]. Compared with the Ni/SBA-15 catalyst, the 350–450 nm band for the other three catalysts shifted slightly to higher wavelength, indicating a lower energy needed for the same electron transfer. This red shift suggested that the addition of Ce and/or Zr weakened Ni–support interaction and thus promoted Ni reduction, which was consistent with the results from H_2 TPR. It is noteworthy that the interaction between Ni and support was weakened to some extent, but it did not worsen Ni dispersion.

3.8. Catalytic activity and selectivity

The WGS catalytic performance of the catalysts was tested from 250 to 500 °C with an interval temperature of 50 °C, presented in Fig. 10 with error bars. At lower temperature, $\leq$300 °C, Ni/SBA-15 catalyst was more active than Ni/Zr–Ce-SBA-15, Ni/Ce-SBA-15, and Ni/Zr-SBA-15 catalysts (Fig. 10a). The calculated equilibrium CO conversion of 98.1% was achieved by Ni/Zr–Ce-SBA-15 catalyst at 400 °C, while Ni/SBA-15, Ni/Ce-SBA-15, and Ni/Zr-SBA-15 catalysts almost attained equilibrium CO conversion of 95.5, 94.7, and 94.6%, respectively. Besides considering WGS activity in term of CO conversion, selectivity toward the WGS reaction was also examined. Fig. 10b reveals the CH_4 and H_2 yields at 250–500 °C for all catalysts. CH_4 formation increased markedly at around 350–400 °C and dropped rapidly above 400 °C, supposedly due to the occurrence of CH_4 steam reforming (see the Supporting Information). Ni/SBA-15 catalyst exhibited the highest CH_4 yield throughout the reaction temperature range and derived a CH_4 yield of 2.5% at 400 °C. It has been reported that carbon monoxide can be disproportionated to form carbon dioxide and adsorbed carbon, and then subsequent hydrogenation of deposited carbon can occur to generate CH_4 [56]. With the incorporation of either Ce or Zr, CH_4 yields decreased slightly to 2.3 and 2.1% at 400 °C for Ni/Ce-SBA-15 and Ni/Zr-SBA-15 catalysts, respectively. Ni/Zr–Ce-SBA-15 catalyst considerably suppressed CH_4 yield over the temperature range. At 400 °C, Ni/Zr–Ce-SBA-15 catalyst achieved a CH_4 yield of 0.4%, which was fivefold lower than that of Ni/SBA-15 catalyst. The highest H_2 yield was also achieved by the Ni/Zr–Ce-SBA-15 catalyst, indicating its high selectivity toward the WGS reaction.

As shown in Fig. 11, the catalytic stability was determined at 400 °C for Ni/Zr-Ce-SBA-15 catalyst in terms of percentage of CO conversion and CH_4 percentage yield. It was observed that the catalyst had stable performance, attaining the equilibrium CO conversion throughout the 70 h. High selectivity toward the WGS reaction was also maintained during the time period, as CH_4 yield was approximately 0.2%. The spent Ni/Zr–Ce-SBA-15 catalyst was further characterized by TEM. Fig. 6e shows the TEM image of spent Ni/Zr–Ce-SBA-15 after 70 h of WGS reaction. The hexagonal array of SBA-15 silica was still observed. As reported by Shanmugam et al. and Takahashi et al., the formation of Si—O—Ce and Si—O—Zr bonds could impede the hydrolysis of Si—O—Si bonds, thereby improving the steam resistance of silica at high temperature. Moreover, no significant sintering of Ni particles was identified, and the average Ni particle size measured from TEM and Ni crystallite size determined from XRD pattern (Fig. S4) increased marginally from 4.1 to 4.4 nm and from 4.6 to 5.2 nm, respectively. TGA analysis (Fig. S5) also revealed no carbon deposition on the spent catalyst.

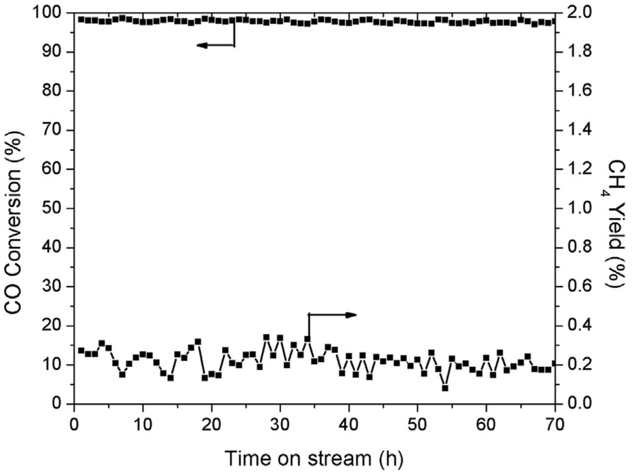

Fig. 11. Percentage of CO conversion and CH_4 percentage yield for Ni/Zr–Ce-SBA-15 catalyst (reaction conditions: 5% CO, 25% H_2O, balance He; W = 50 mg; reaction temperature 400 °C; 70 h).

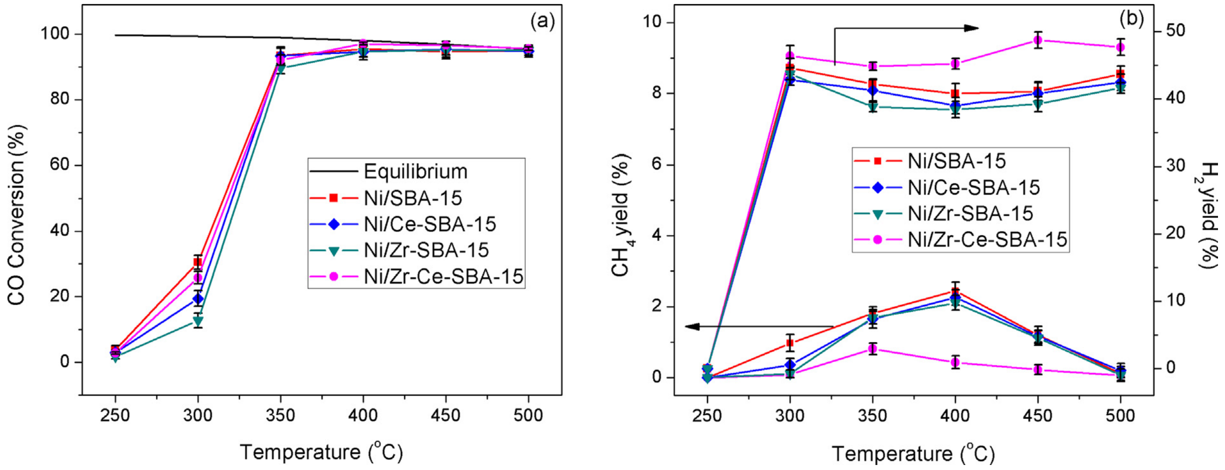

Fig. 10. (a) Percentage of CO conversion and (b) CH_4 and H_2 percentage yields for the four catalysts (reaction conditions: 5% CO, 25% H_2O, balance He; W = 30 mg; reaction temperature 250–500 °C).

The activity of Ni/SBA-15 and Ni/Zr–Ce-SBA-15 catalysts is compared with that of other catalysts reported in the literature in Table 3. TOF values and H_2 formation rates were obtained according to the procedure reported in Ashok et al. [10]. In this system at 375 °C, Ni/SBA-15 and Ni/Zr–Ce-SBA-15 catalysts showed TOF values of 3.50 and 4.57 s^{-1} and H_2 formation rates of 343 and 534 μmol $H_2/g_{cat}s^{-1}$, respectively. Ni/SBA-15 catalyst had a higher TOF value than Ni/SiO_2 and Ni/SiO_{2p}[6 0 0] catalysts tested under the same conditions [10]; however, the H_2 formation rate for the Ni/SBA-15 catalyst was lower than that of the Ni/SiO_{2p}[6 0 0] catalyst. The best catalyst in the present work, Ni/Zr–Ce-SBA-15, showed superior performance in terms of TOF and H_2 formation rate as compared to Ni/SiO_{2p}[6 0 0] catalyst and other Ni-based catalysts [14,18,57,58] at a high reaction temperature of $\geq$300 °C. The methanation reaction rate was also measured over Ni/SBA-15 and Ni/Zr–Ce-SBA-15 catalysts under WGS conditions in which methane formation was observed (shown in the Supporting Information). The methanation reaction rates of Ni/SBA-15 and Ni/Zr–Ce-SBA-15 catalysts were 3.6×10^{-4} and 1.6×10^{-4} s^{-1}, respectively. These kinetic data were consistent with catalytic performance, indicating the positive effect of Zr and Ce co-presence on methanation suppression. Thus, highly active and selective Ni/Zr–Ce-SBA-15 catalyst can be utilized for the WGS reaction, especially at high temperatures.

3.9. CO diffuse reflectance infrared Fourier transform spectroscopy analysis

The surface-active species on the reduced catalysts during the WGS reaction were investigated using *in situ* DRIFTS analysis under a continuous flow of CO gas. In Fig. 12, the DRIFTS spectra of CO adsorption over all reduced catalysts are shown. The wavenumber and mode assignments for the reduced catalysts are summarized in Table 4.

In the hydroxyl region, one main peak at 3747 cm^{-1} was observed for all samples, which can be assigned to terminal hydroxyl (—OH) groups on the silica surface [59]. As the temperature was increased, the consumption of these OH groups was clearly visible, revealing their participation in the reaction. In the carbonylic region, the literature typically reported two bands at around 2013 and 2035 cm^{-1} at low temperature (50–200 °C), which can be attributed to linear CO adsorbed on Ni and linear CO adsorbed on hydrogen-modified Ni. However, no linear CO adsorption was detected in this catalytic system; instead, subcarbonyl nickel species $Ni(CO)_n$ (n = 2 or 3) were observed. In Fig. 12a, the band at 2074 cm^{-1} corresponding to subcarbonyl nickel species appears at 200 °C. This peak attained the maximum intensity at 300 °C and then was red-shifted down to 2054 cm^{-1} with lower intensity as temperature was increased to 400 °C. Above 400 °C, this band eventually disappeared, while the bands associated with gaseous CO_2 exhibited higher intensity. As reported by Ang et al., these subcarbonyl nickel species are identified as the precursor for the CO methanation reaction, producing CO_2 (g) and CH_4 (g) [14]. Ang et al. also reported the concomitant consumption of subcarbonyls and OH groups for the Ni/SiO_2 (OA) catalyst [19]. These findings were consistent with high CO conversion along with high CH_4 yield at 250–350 °C for Ni/SBA-15, presented in Fig. 10a and b. The DRIFTS spectra of the reduced Ni/Ce-SBA-15 and Ni/Zr-SBA-15 catalysts are presented in Fig. 12b and c, respectively. For these two catalysts, the appearance of subcarbonyl nickel species was obvious at 250 °C, followed by the same trend as found in Ni/SBA-15 but with lower intensity. This observation was well supported by slightly lower CH_4 yield (Fig. 10b). For Ni/Zr–Ce-SBA-15, the bands in both hydroxyl and carbonyl regions also appeared in the CO DRIFTS spectra (Fig. 12d). Although the subcarbonyl nickel species was still present, the intensity was much lower than in spectra of other catalysts and the band vanished above 350 °C. When the wavenumbers of the subcarbonyl species on four catalysts at 350 °C are compared (Table 4), that for Ni/Zr–Ce-SBA-15 catalyst was lower (2054 cm^{-1}) indicating that CO was more strongly adsorbed on this catalyst [19]. The stronger CO adsorption also made for less carbon deposition by CO dissociation and subsequent formation of surface carbonaceous species, and thus fewer precursors for methane formation [60]. Apart from subcarbonyl species, carbonyl species in the bridged and multibonded configurations were also visible at 1930 and 1820 cm^{-1}, respectively. These lower frequencies of bridging and multibonding modes represent a weaker CO bond, implying CO held more strongly by Ni [61,62]. In the carbonate region, three bands situated at around 1578, 1284, and 1101 cm^{-1} were present at low temperature in the spectra of all samples, and can be attributed to bidentate carbonate species [9]. As the temperature was increased, the intensity of these bands remained constant for Ni/SBA-15 and Ni/Ce-SBA-15 catalysts. In contrast, these species (at around 1576 and 1572 cm^{-1}) were detected in small amounts in Ni/Zr-SBA-15 and Ni/Zr–Ce-SBA-15 catalysts, possibly due to the conversion of bidentate carbonates to CO_2 (g) [19].

The *in situ* DRIFTS WGS reaction was also performed over Ni/SBA-15 and Ni/Zr–Ce-SBA-15 catalysts to provide more precise insights. Evolution of active species similar to those in CO adsorption studies is presented in Fig. 13. Subcarbonyl species (2067 cm^{-1}) appeared at 300 °C and reached maximum intensity at 350 °C in the spectra of the Ni/SBA-15 catalyst. Upon temperature increment, subcarbonyl species disappeared, along with substantial formation of CO_2 (g) and CH_4 (g). Interestingly, linear carbonyls (2040 cm^{-1}), absent during CO adsorption, were evident at 400 °C and diminished at >400 °C under WGS conditions. Much weaker intensities of subcarbonyl species (2061 cm^{-1}) as well as CH_4 (g) were found in the spectra of the Ni/Zr–Ce-SBA-15 catalyst. Linear carbonyls (2030 cm^{-1}) were also detectable at 400 °C, and a considerable decrease in their intensities at >400 °C was accompanied by an intensity increase of CO_2 (g).

3.10. CO temperature-programmed reduction–mass spectroscopy

CO-TPR was utilized to identify surface oxygen and hydroxyl species from the support in the WGS reaction. Prior to the analysis,

Table 3
Comparison of WGS reaction rates in this work with the values in the literature.

Catalyst	Conditions	Temperature (°C)	TOF (s^{-1})	Rate (μmol $H_2/g_{cat}s^{-1}$)	Reference
Ni/SBA-15	5% CO,25% H_2O, balance He	375	3.50	343	This work
Ni/Zr–Ce-SBA-15	5% CO, 25% H_2O, balance He	375	4.57	534	This work
Ni/SiO_2	5% CO, 25% H_2O, balance He	375	1.1	141	[10]
Ni/SiO_{2p}[600]	5% CO, 25% H_2O, balance He	375	2.79	493	[10]
5Ni5Cu/CeO_2	7% CO, 22% H_2O, 10% CO_2, 20% H_2, balance He	350	0.013	19	[18]
Ni/2Na/CeO_2	7% CO, 22% H_2O, 10% CO_2, 20% H_2, balance He	400	0.46	75	[14]
1Re-10Ni/CeO_2	5% CO, 10% H_2O, balance He	300		30	[57]
$Ni_{20}/CeLaO_x$	10% CO, 20% H_2O, balance He	400		36	[58]

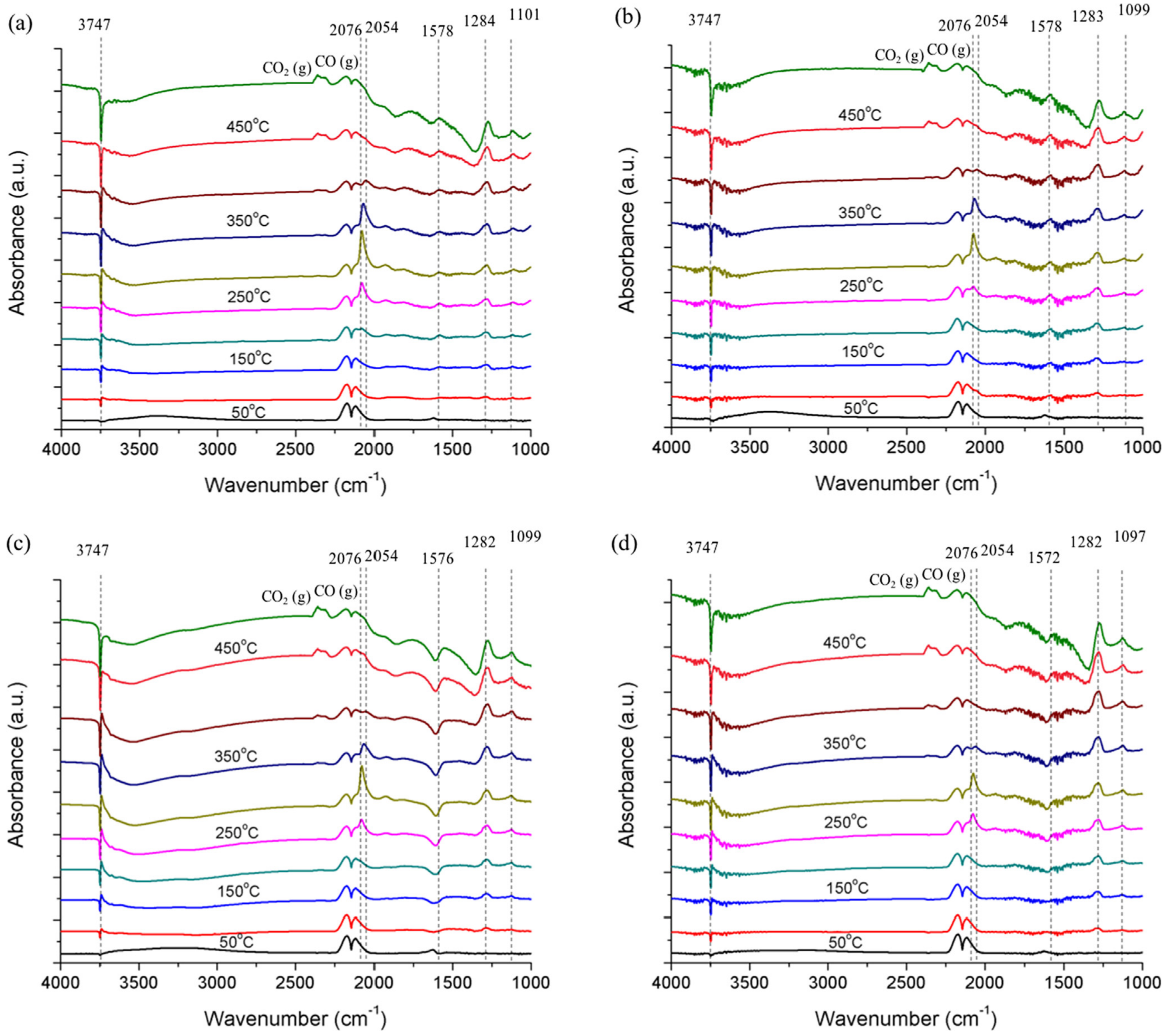

Fig. 12. *In situ* DRIFTS CO adsorption study on (a) Ni/SBA-15, (b) Ni/Ce-SBA-15, (c) Ni/Zr-SBA-15, and (d) Ni/Zr–Ce-SBA-15 catalysts at temperature increments of 50 °C.

Table 4
Wavenumber and mode assignments for the reduced catalysts during CO DRIFTS analysis.

Surface species	Wavenumber (cm^{-1}) literature value	Ni/SBA-15	Ni/Ce-SBA-15	Ni/Zr-SBA-15	Ni/Z–Ce-SBA-15
Surface hydroxyl					
Terminal –OH	3747	3747	3747	3747	3747
Surface carbonyl					
Subcarbonyl	2080–2050	2076 (200–300 °C) 2071 (350 °C) 2054 (400 °C)	2076 (250–300 °C) 2071 (350 °C) 2054 (400 °C)	2076 (250 °C) 2071 (300 °C) 2068 (350 °C) 2054 (400 °C)	2076 (250 °C) 2068 (300 °C) 2054 (350 °C)
Bridged	1950–1880	1930	1930	1930	1930
Multibonded	1875–1800	1820	1820	1820	1820
Surface carbonate					
Bidentate carbonate	1562, 1286, 1101	1578, 1284, 1101	1578, 1283, 1099	1576, 1282, 1099	1572, 1282, 1097

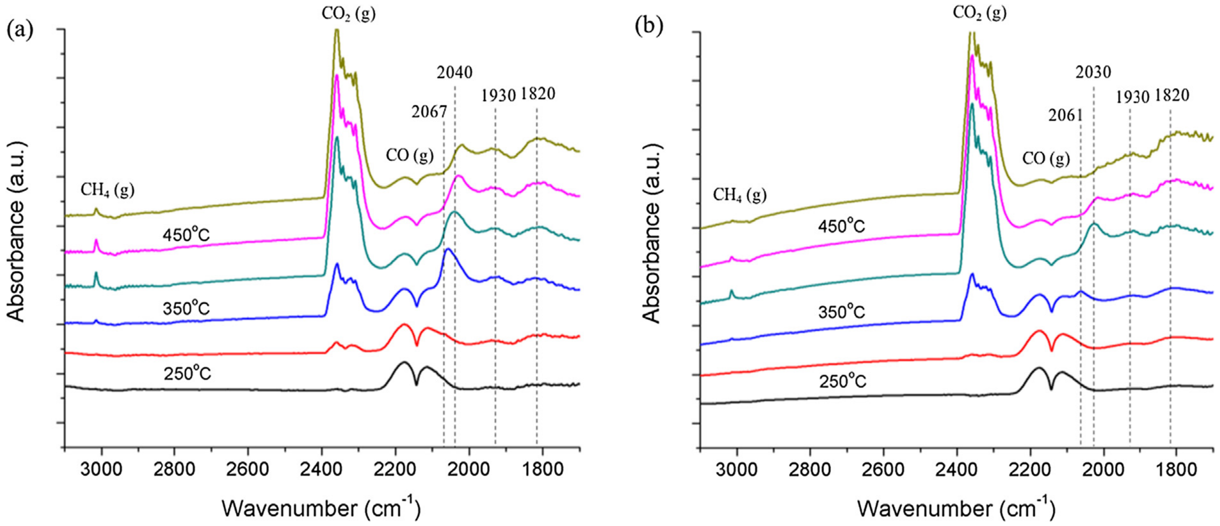

Fig. 13. *In situ* DRIFTS WGS reaction study on (a) Ni/SBA-15 and (b) Ni/Zr–Ce-SBA-15 catalysts (4000–1000 cm^{-1} in the Supporting Information).

the catalysts were reduced under the same conditions as those tested during the WGS reaction so that the CO behavior on the reduced catalysts could be discerned. It has been reported that these oxygen species are postulated to be involved in WGS reaction mechanisms. CO may react with hydroxyl groups present in the silica support or formed on partially reduced supported such as CeO_2 to form CO_2 and H_2 [63]:

$$CO(ads) + 2OH\,(support) \rightarrow CO_2\,(g) + H_2\,(g) + O_L. \tag{7}$$

In addition, CO disproportionation,

$$2CO \rightarrow CO_2\,(g) + C, \tag{8}$$

and oxidization of CO by surface lattice oxygen (O_L),

$$CO + O_L \rightarrow CO_2\,(g), \tag{9}$$

can be routes for CO_2 production [64].

Fig. 14a, b, and c depict the CO consumption, CO_2 production, and H_2 production, respectively, for the reduced Ni/SBA-15 and Ni/Zr–Ce-SBA-15 catalysts. It has been reported that the reducible surface oxygen species present in the catalyst could react with CO to produce CO_2 at temperatures around 100–250 °C [65]. Significant numbers of OH groups were activated at higher temperatures above 320 °C [66]. In particular, two main H_2 production peaks could be discerned at about 330 and 470 °C. H_2 evolution roughly coincided with CO_2 production, indicating the reaction between CO and surface OH groups (7) in this temperature range. The maximum CO consumption and CO_2 production peaks for both catalysts centered at approximately 470 °C could be due to the combination of the CO reaction with both surface OH groups (7) and surface oxygen species (9) [67]. The peak of the H_2 signal at 470 °C was weakened, possibly due to the diminution of OH groups present in the samples [63]. These consumed surface OH groups were reported to be labile and regenerated from H_2O dissociation on active nickel, forming Ni–OH again [10]. When the two catalysts are compared, CO disproportionation (8) was more likely to occur on Ni/SBA-15 catalyst, as shown by higher intensity of subcarbonyl nickel species in DRIFTS spectra. Furthermore, the Ni/Zr–Ce-SBA-15 catalyst showed higher H_2 production than the Ni/SBA-15 catalyst. More H_2 evolved from the surface WGS reaction indicated that ample OH groups participated in this reaction. These active surface hydroxyls may be present in the support and formed on partially reduced ceria/zirconia.

4. Kinetic study of the Ni/Zr–Ce-SBA-15 catalyst

Generally, two mechanisms have been proposed for the WGS reaction, an associative mechanism and a redox mechanism. In the associative mechanism, a formate species (HCOO) as an active intermediate is produced from adsorbed CO and dissociated —OH groups, followed by decomposition to CO_2 and H_2 [68,69]. Apart from formate as the intermediate species, formation of carboxyl (COOH) intermediates has been proposed through the reaction of adsorbed CO with adsorbed OH, in which hydrogen is bonded to oxygen [70,71]. In the redox mechanism, adsorbed oxygen on the support can react with adsorbed CO on the metal site, producing CO_2. The support is then reoxidized by steam to generate H_2 [72–75]. In the present study, no formates were observed during *in situ* DRIFTS study for the Ni/Zr–Ce-SBA-15 catalyst. Therefore, two relevant kinetic models, carboxyl and redox, were derived and fitted to the kinetic experimental data.

The WGS reaction orders in CO, H_2O, CO_2, and H_2 were first obtained by evaluating the effect of partial pressures of reactants (CO and H_2O) and products (CO_2 and H_2) on the reaction rate over the Ni/Zr–Ce-SBA-15 catalyst at 375 °C. Based on the kinetic rate, the apparent reaction order was calculated. As shown in Fig. 15, the WGS reaction orders with respect to CO, H_2O, CO_2, and H_2 were found to be 0.9, 0.3, −0.2, and −0.3, respectively. Thus, the overall rate was expressed in the form of a power rate law,

$$r = A\exp\left(\frac{-E_a}{RT}\right)[P_{CO}]^{0.9}\left[P_{H_2O}\right]^{0.3}\left[P_{CO_2}\right]^{-0.2}\left[P_{H_2}\right]^{-0.3}(1-\beta), \tag{10}$$

where $\beta = \frac{[CO_2][H_2]}{[CO][H_2O]K_{eq}}$ and $K_{eq} = \exp(\frac{4577.8}{T} - 4.33)$.

Table 5 compares reaction orders with literature values over other catalysts. The apparent reaction orders for the Ni/Zr–Ce-SBA-15 catalyst in this study also exhibited great similarity to those for 10 at.% Cu—Ce (30 at.% La)O_x catalyst [76] and 5Ni5Cu/CeO_2 catalyst [18], particularly at high temperature. These results indicated weak inhibitory effects of both CO_2 and H_2 on the reaction. Almost first-order dependence of the reaction rate on partial pressure of CO also revealed the relatively weak adsorption of CO [77], while the reaction order in H_2O was indicative of a surface saturated with hydroxyls [78].

The kinetic experimental data were further fitted with redox and carboxyl kinetic models to elucidate the reaction mechanism. The derivation of the dual-site carboxyl mechanism is shown in the Supporting Information. A R^2 value of 0.92 was achieved for the

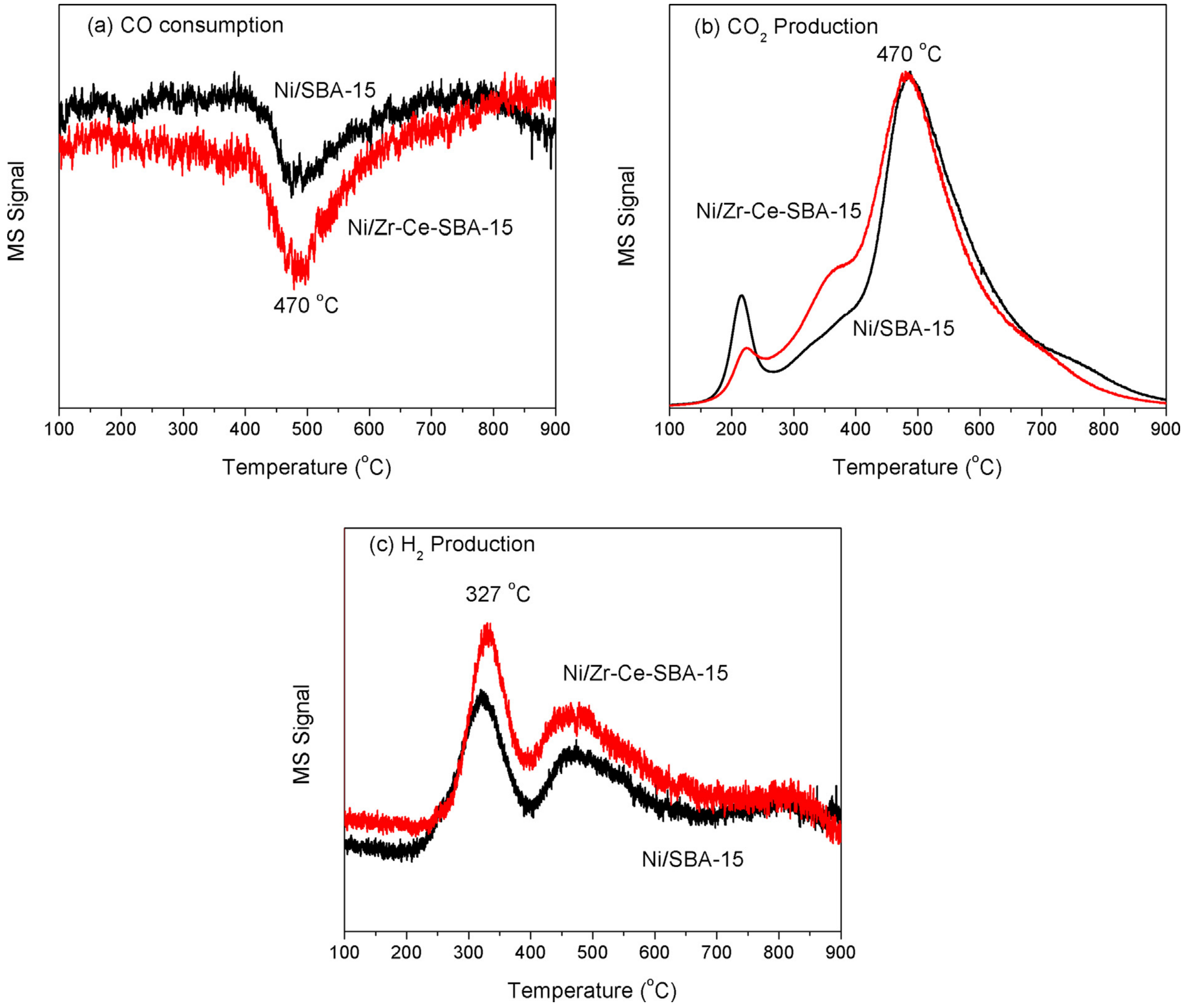

Fig. 14. TPR-CO-MS for (a) CO consumption, (b) CO_2 production, and (c) H_2 production.

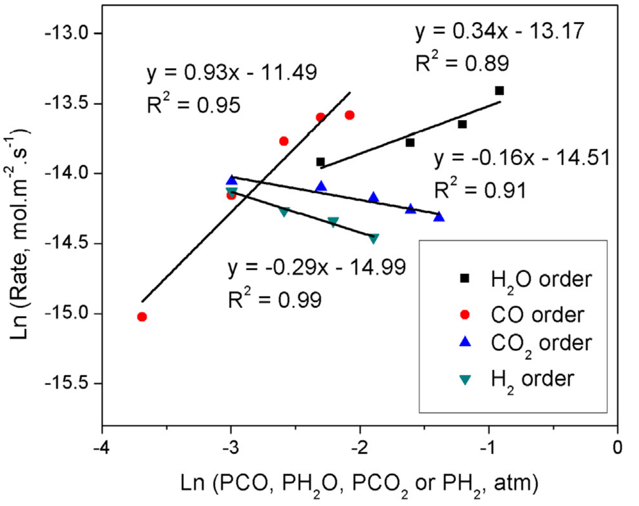

Fig. 15. Determination of power law kinetic rate model by varying partial pressures of CO, H_2O, CO_2, and H_2 over the Ni/Zr–Ce-SBA-15 catalyst at 375 °C.

best fit (Fig. S1), in which the fitted parameters from this mechanism was found to be within the imposed constraints (Table S1). The kinetic study shows that the proposed dual-site carboxyl mechanism is plausible for this catalytic system. This implied that hydroxyl species available from the silica support and from the reaction of steam with oxygen vacancies of ceria and zirconia participated in the WGS reaction by reacting directly with CO to form COOH species, which subsequently decompose to CO_2 and H_2. Vlachos et al. performed a systematic density functional theory (DFT) study of the WGS reaction on Ni(1 1 1) surfaces and also reported that the carboxyl pathway was favored, with $CO^* + OH^* \rightleftharpoons COOH^* + {}^*$ as the rate-determining step [81]. In another study, Zhou and Liu used periodic DFT calculations to investigate the competition of the WGS reaction versus methanation on clean and K-modified Ni(1 1 1) surfaces [82]. Redox and carboxyl pathways are both kinetically competitive on clean Ni(1 1 1), whereas the carboxyl pathway benefits from the presence of K adatoms. It has been reported that alkali-modified Ni catalysts have an increase in hydroxyl concentration, and the associative mechanism is probably more dominant than the redox mechanism due to the surface hydroxyl enrichment [12,83,84]. The carboxyl mechanism has also been proposed in other catalytic systems with the participation of surface OH groups in the WGS reaction [18,77,85]. Hence, the carboxyl mechanism is the most plausible pathway for the Ni–phyllosilicate structure-derived Ni/Zr–Ce-SBA-15 catalyst with high density of the active hydroxyls, even though only a simple kinetic model was used for data fitting in this study.

Table 5
Literature values for reaction orders of WGS reaction.

Catalyst	T (°C)	Reaction orders				Reference
		CO	H_2O	CO_2	H_2	
Ni/Zr–Ce-SBA-15	375	0.9	0.3	–0.2	–0.3	This work
$5Ni5Cu/CeO_2$	375	1.0	0.2	–0.3	–0.2	[18]
$Ni/5K/CeO_2$	400	0.2	0.6	–0.2	–0.5	[9]
10 at.% Cu–Ce(30 at.% La)O_x	450	0.8	0.2	–0.3	–0.3	[76]
1% Pt/Al_2O_3	315	0.1	1.0	–0.1	–0.5	[79]
0.5% Pt–0.5% Re/TiO_2	300	0.4	0.7	0.0	–0.4	[80]

5. Role of Ce and Zr ions in the silica matrix

The catalytic activity test showed that all Ni-based SBA-15 catalysts exhibited high CO conversion, especially above 350 °C. The reason was the presence of ample OH groups and their participation in the WGS reaction, as seen from *in situ* DRIFTS. When the selectivity toward the WGS reaction is compared, it is clear that the existence of heteroatom(s) could suppress undesired methanation. Furthermore, a better suppression effect of Ni-based SBA-15 catalyst containing two heteroatoms than those containing one heteroatom may imply interaction between ceria and zirconia, possibly incorporated adjacently within the silica framework. As investigated by *in situ* DRIFTS CO adsorption, the co-presence of Ce and Zr ions reduced the formation of subcarbonyl nickel species, and also created a red shift of the CO adsorption band, representing a weaker CO bond. The explanation for this lower-frequency shift might be that the unfilled *d*-orbitals of Ni atoms accepted *d*-electrons from Ce, leading to an increase in *d*-electron density of Ni atoms. The interaction between Ni and Zr also caused Ni atoms to maintain an electron-rich character. Hence, electron-rich Ni sites enhanced back-donation from Ni to the antibonding π-state of the CO molecule, from which a weakening of the CO bond would be expected [86]. This weaker CO bond may imply that CO adsorbed strongly on Ni atoms. It was reported that carbon deposition through CO disproportionation occurred less readily on the sites for more strongly held CO [60]. Less tendency for formation of carbon precursors thus impeded subsequent hydrogenation to form CH_4.

6. Conclusions

In this study, zirconium- and/or cerium-incorporated mesoporous silica SBA-15 synthesized via one-pot hydrothermal synthesis were chosen as supports to prepare Ni–phyllosilicate-derived catalysts for the WGS reaction. As evidenced by characterization results, all catalysts possessed high surface area and a well-ordered hexagonal array of the channels, in which Ni particles were uniformly dispersed. *In situ* CO DRIFTS studies revealed high negative peaks in the hydroxyl region for all catalysts, suggesting the consumption of OH groups by reaction with CO to produce CO_2 and H_2. In addition, the formation of subcarbonyl nickel species was minimized with the incorporation of metal ions, Ce and Zr, into SBA-15. It was also found that CO was adsorbed more strongly on the Ni/Zr–Ce-SBA-15 catalyst at high temperature, which in turn could prevent CO dissociation and subsequent hydrogenation to form CH_4. The best catalyst in this work, Ni/Zr–Ce-SBA-15, achieved excellent catalytic activity in the WGS reaction in terms of turnover frequency ($4.57\ s^{-1}$) and hydrogen formation rate ($534\ \mu mol\ H_2\ g^{-1}s^{-1}$). Also, it showed stable performance, attaining equilibrium CO conversion and high selectivity toward the WGS reaction throughout the 70 h. The kinetic study revealed weak product inhibitions toward the reaction rate. Additionally, the dual-site carboxyl mechanism could be a dominant reaction pathway for the Ni/Zr–Ce-SBA-15 catalyst.

Methanation kinetic measurements, constraints imposed on kinetic data fitting (Table S1), validation of the kinetic model, comparison of experimental rate and calculated rate of the dual-site carboxyl model for the Ni/Zr–Ce-SBA-15 catalyst (Fig. S1), estimated kinetic parameters for the proposed carboxyl model (Table S2), catalytic activity in steam reforming of methane (Fig. S2), catalytic activity testing under condition for low CO conversion (Fig. S3), XRD pattern (Fig. S4) and TGA profile (Fig. S5) of spent Ni/Zr–Ce-SBA-15 catalyst after 70 h of reaction, and an *in situ* DRIFTS WGS reaction study in the wavenumber range 4000–1000 cm^{-1} (Fig. S6) are provided in the Supporting Information.

Declaration of Competing Interest

Acknowledgments

The authors gratefully thank the National University of Singapore, the National Environment Agency of Singapore (NEA-ETRP Grant 1501 103, WBS R-279-000-491-279), the Agency for Science, Technology and Research (AME-IRG A1783c0016, WBS R-279-000-509-305), and the Ministry of Education (MOE 2017-T2-2-130, WBS R-279-000-544-112) for generously supporting this work. The authors also thank Professor Fabio H. Ribeiro for providing facilities for STEM-HAADF and methanation kinetic measurements and giving valuable suggestions. This contribution is based upon work supported in part by the National Science Foundation under Cooperative Agreement EEC-1647722. The authors declare no competing financial interests.

Appendix A. Supplementary material

Supplementary data to this article can be found online at https://doi.org/10.1016/j.jcat.2019.11.042.

References

[1] D.B. Pal, R. Chand, S.N. Upadhyay, P.K. Mishra, Performance of water gas shift reaction catalysts: A review, Renew. Sust. Energ. Rev. 93 (2018) 549–565.
[2] M. Zhu, I.E. Wachs, Iron-based catalysts for the high-temperature water–gas shift (HT-WGS) reaction: A review, ACS Catal. 6 (2016) 722–732.
[3] L. Gradisher, B. Dutcher, M. Fan, Catalytic hydrogen production from fossil fuels via the water gas shift reaction, Appl. Energy 139 (2015) 335–349.
[4] A. Ambrosi, S.E. Denmark, Harnessing the power of the water-gas shift reaction for organic synthesis, Angew. Chem. Int. Ed. 55 (2016) 12164–12189.
[5] S. Li, J. Gong, Strategies for improving the performance and stability of Ni-based catalysts for reforming reactions, Chem. Soc. Rev. 43 (2014) 7245–7256.
[6] Y. Kathiraser, J. Ashok, S. Kawi, Synthesis and evaluation of highly dispersed SBA-15 supported Ni–Fe bimetallic catalysts for steam reforming of biomass derived tar reaction, Catal. Sci. Technol. 6 (2016) 4327–4336.
[7] J. Ashok, Y. Kathiraser, M.L. Ang, S. Kawi, Ni and/or Ni–Cu alloys supported over SiO2 catalysts synthesized via phyllosilicate structures for steam reforming of biomass tar reaction, Catal. Sci. Technol. 5 (2015) 4398–4409.

[8] H. Ma, L. Zeng, H. Tian, D. Li, X. Wang, X. Li, J. Gong, Efficient hydrogen production from ethanol steam reforming over La-modified ordered mesoporous Ni-based catalysts, Appl. Catal. B 181 (2016) 321–331.

[9] M.L. Ang, U. Oemar, Y. Kathiraser, E.T. Saw, C.H.K. Lew, Y. Du, A. Borgna, S. Kawi, High-temperature water–gas shift reaction over Ni/xK/CeO2 catalysts: Suppression of methanation via formation of bridging carbonyls, J. Catal. 329 (2015) 130–143.

[10] J. Ashok, M.L. Ang, P.Z.L. Terence, S. Kawi, Promotion of the water-gas-shift reaction by nickel hydroxyl species in partially reduced nickel-containing phyllosilicate catalysts, ChemCatChem 8 (2016) 1308–1318.

[11] A. Jha, D.-W. Jeong, W.-J. Jang, Y.-L. Lee, H.-S. Roh, Hydrogen production from water–gas shift reaction over Ni–Cu–CeO2 oxide catalyst: The effect of preparation methods, Int. J. Hydrogen Energy 40 (2015) 9209–9216.

[12] J. Ashok, M.H. Wai, S. Kawi, Nickel-based catalysts for high-temperature water gas shift reaction-methane suppression, ChemCatChem 10 (2018) 3927–3942.

[13] D. Damma, P.G. Smirniotis, Recent advances in iron-based high-temperature water-gas shift catalysis for hydrogen production, Curr. Opin. Chem. Eng. 21 (2018) 103–110.

[14] M.L. Ang, U. Oemar, E.T. Saw, L. Mo, Y. Kathiraser, B.H. Chia, S. Kawi, Highly active Ni/xNa/CeO2 catalyst for the water–gas shift reaction: Effect of sodium on methane suppression, ACS Catal. 4 (2014) 3237–3248.

[15] T. Maneerung, K. Hidajat, S. Kawi, K-doped LaNiO3 perovskite for high-temperature water-gas shift of reformate gas: Role of potassium on suppressing methanation, Int. J. Hydrogen Energy 42 (2017) 9840–9857.

[16] Y.-L. Lee, A. Jha, W.-J. Jang, J.-O. Shim, C.V. Rode, B.-H. Jeon, J.W. Bae, H.-S. Roh, Effect of alkali and alkaline earth metal on Co/CeO2 catalyst for the water-gas shift reaction of waste derived synthesis gas, Appl. Catal. A 551 (2018) 63–70.

[17] F. Meshkani, M. Rezaei, Mesoporous Ba-promoted chromium free Fe2O3–Al2O3–NiO catalyst with low methanation activity for high temperature water gas shift reaction, Catal. Commun. 58 (2015) 26–29.

[18] E.T. Saw, U. Oemar, X.R. Tan, Y. Du, A. Borgna, K. Hidajat, S. Kawi, Bimetallic Ni–Cu catalyst supported on CeO2 for high-temperature water–gas shift reaction: Methane suppression via enhanced CO adsorption, J. Catal. 314 (2014) 32–46.

[19] M.L. Ang, J.T. Miller, Y. Cui, L. Mo, S. Kawi, Bimetallic Ni–Cu alloy nanoparticles supported on silica for the water-gas shift reaction: activating surface hydroxyls via enhanced CO adsorption, Catal. Sci. Technol. 6 (2016) 3394–3409.

[20] E.T. Saw, U. Oemar, M.L. Ang, K. Hidajat, S. Kawi, Highly active and stable bimetallic nickel–copper core–ceria shell catalyst for high-temperature water–gas shift reaction, ChemCatChem 7 (2015) 3358–3367.

[21] C. Ciotonea, B. Dragoi, A. Ungureanu, A. Chirieac, S. Petit, S. Royer, E. Dumitriu, Nanosized transition metals in controlled environments of phyllosilicate-mesoporous silica composites as highly thermostable and active catalysts, Chem. Commun. 49 (2013) 7665–7667.

[22] B. Lu, K. Kawamoto, Transition metal-rich mesoporous silicas and their enhanced catalytic properties, Catal. Sci. Technol. 4 (2014) 4313–4321.

[23] U. Oemar, Y. Kathiraser, M.L. Ang, K. Hidajat, S. Kawi, Catalytic biomass gasification to syngas over highly dispersed lanthanum-doped nickel on SBA-15, ChemCatChem 7 (2015) 3376–3385.

[24] X. Wu, S. Kawi, Rh/Ce-SBA-15: Active and stable catalyst for CO2 reforming of ethanol to hydrogen, Catal. Today 148 (2009) 251–259.

[25] S. Kawi, Y. Kathiraser, J. Ni, U. Oemar, Z. Li, E.T. Saw, Progress in synthesis of highly active and stable nickel-based catalysts for carbon dioxide reforming of methane, ChemSusChem 8 (2015) 3556–3575.

[26] Z. Bian, S. Das, M.H. Wai, P. Hongmanorom, S. Kawi, A review on bimetallic nickel-based catalysts for CO2 reforming of methane, ChemPhysChem 18 (2017) 3117–3134.

[27] Z. Li, S. Das, P. Hongmanorom, N. Dewangan, M.H. Wai, S. Kawi, Silica-based micro- and mesoporous catalysts for dry reforming of methane, Catal. Sci. Technol. 8 (2018) 2763–2778.

[28] S. Aranifard, S.C. Ammal, A. Heyden, On the importance of metal–oxide interface sites for the water–gas shift reaction over Pt/CeO2 catalysts, J. Catal. 309 (2014) 314–324.

[29] P.O. Graf, D.J.M. de Vlieger, B.L. Mojet, L. Lefferts, New insights in reactivity of hydroxyl groups in water gas shift reaction on Pt/ZrO2, J. Catal. 262 (2009) 181–187.

[30] S.C. Ammal, A. Heyden, Origin of the unique activity of Pt/TiO2 catalysts for the water–gas shift reaction, J. Catal. 306 (2013) 78–90.

[31] C. Wen, Y. Zhu, Y. Ye, S. Zhang, F. Cheng, Y. Liu, P. Wang, F. Tao, Water–gas shift reaction on metal nanoclusters encapsulated in mesoporous ceria studied with ambient-pressure X-ray Photoelectron Spectroscopy, ACS Nano 6 (2012) 9305–9313.

[32] M. Xu, S. He, H. Chen, G. Cui, L. Zheng, B. Wang, M. Wei, TiO2−x-modified Ni nanocatalyst with tunable metal–support interaction for water–gas shift reaction, ACS Catal. 7 (2017) 7600–7609.

[33] E.C. Vagia, A.A. Lemonidou, Investigations on the properties of ceria–zirconia-supported Ni and Rh catalysts and their performance in acetic acid steam reforming, J. Catal. 269 (2010) 388–396.

[34] E. del Río, D. Gaona, J.C. Hernández-Garrido, J.J. Calvino, M.G. Basallote, M.J. Fernández-Trujillo, J.A. Pérez-Omil, J.M. Gatica, Speciation-controlled incipient wetness impregnation: A rational synthetic approach to prepare sub-nanosized and highly active ceria–zirconia supported gold catalysts, J. Catal. 318 (2014) 119–127.

[35] M. Moser, G. Vilé, S. Colussi, F. Krumeich, D. Teschner, L. Szentmiklósi, A. Trovarelli, J. Pérez-Ramírez, Structure and reactivity of ceria–zirconia catalysts for bromine and chlorine production via the oxidation of hydrogen halides, J. Catal. 331 (2015) 128–137.

[36] O.A. González Vargas, J.A. de los Reyes Heredia, J.A. Wang, L.F. Chen, A. Montesinos Castellanos, M.E. Llanos, Hydrogen production over Rh/Ce-MCM-41 catalysts via ethanol steam reforming, Int. J. Hydrogen Energy 38 (2013) 13914–13925.

[37] R. Takahashi, S. Sato, T. Sodesawa, M. Yoshida, S. Tomiyama, Addition of zirconia in Ni/SiO2 catalyst for improvement of steam resistance, Appl. Catal. A 273 (2004) 211–215.

[38] V. Shanmugam, R. Zapf, S. Neuberg, V. Hessel, G. Kolb, Effect of ceria and zirconia promotors on Ni/SBA-15 catalysts for coking and sintering resistant steam reforming of propylene glycol in microreactors, Appl. Catal. B 203 (2017) 859–869.

[39] D. Zhao, Q. Huo, J. Feng, B.F. Chmelka, G.D. Stucky, Nonionic triblock and star diblock copolymer and oligomeric surfactant syntheses of highly ordered, hydrothermally stable, mesoporous silica structures, J. Am. Chem. Soc. 120 (1998) 6024–6036.

[40] T. Xie, L. Shi, J. Zhang, D. Zhang, Immobilizing Ni nanoparticles to mesoporous silica with size and location control via a polyol-assisted route for coking- and sintering-resistant dry reforming of methane, Chem. Commun. 50 (2014) 7250–7253.

[41] C. Zhang, H. Yue, Z. Huang, S. Li, G. Wu, X. Ma, J. Gong, Hydrogen production via steam reforming of ethanol on phyllosilicate-derived Ni/SiO2: Enhanced metal–support interaction and catalytic stability, ACS Sust. Chem. Eng. 1 (2013) 161–173.

[42] M.V. Sivaiah, S. Petit, J. Barrault, C. Batiot-Dupeyrat, S. Valange, CO2 reforming of CH4 over Ni-containing phyllosilicates as catalyst precursors, Catal. Today 157 (2010) 397–403.

[43] M. Yang, P. Jin, Y. Fan, C. Huang, N. Zhang, W. Weng, M. Chen, H. Wan, Ammonia-assisted synthesis towards a phyllosilicate-derived highly-dispersed and long-lived Ni/SiO2 catalyst, Catal. Sci. Technol. 5 (2015) 5095–5099.

[44] S.-Y. Chen, C.-Y. Tang, W.-T. Chuang, J.-J. Lee, Y.-L. Tsai, J.C.C. Chan, C.-Y. Lin, Y.-C. Liu, S. Cheng, A facile route to synthesizing functionalized mesoporous SBA-15 materials with platelet morphology and short mesochannels, Chem. Mater. 20 (2008) 3906–3916.

[45] Z. Bian, S. Kawi, Preparation, characterization and catalytic application of phyllosilicate: A review, Catal. Today (2018).

[46] N. Wang, K. Shen, L. Huang, X. Yu, W. Qian, W. Chu, Facile route for synthesizing ordered mesoporous Ni–Ce–Al oxide materials and their catalytic performance for methane dry reforming to hydrogen and syngas, ACS Catal. 3 (2013) 1638–1651.

[47] M. Tan, X. Wang, X. Wang, X. Zou, W. Ding, X. Lu, Influence of calcination temperature on textural and structural properties, reducibility, and catalytic behavior of mesoporous γ-alumina-supported Ni–Mg oxides by one-pot template-free route, J. Catal. 329 (2015) 151–166.

[48] J. Kugai, V. Subramani, C. Song, M.H. Engelhard, Y.-H. Chin, Effects of nanocrystalline CeO2 supports on the properties and performance of Ni–Rh bimetallic catalyst for oxidative steam reforming of ethanol, J. Catal. 238 (2006) 430–440.

[49] S. Das, J. Ashok, Z. Bian, N. Dewangan, M.H. Wai, Y. Du, A. Borgna, K. Hidajat, S. Kawi, Silica-Ceria sandwiched Ni core–shell catalyst for low temperature dry reforming of biogas: Coke resistance and mechanistic insights, Appl. Catal. B 230 (2018) 220–236.

[50] D. Baudouin, U. Rodemerck, F. Krumeich, A.D. Mallmann, K.C. Szeto, H. Ménard, L. Veyre, J.-P. Candy, P.B. Webb, C. Thieuleux, C. Copéret, Particle size effect in the low temperature reforming of methane by carbon dioxide on silica-supported Ni nanoparticles, J. Catal. 297 (2013) 27–34.

[51] A. Rodriguez-Gomez, R. Pereñiguez, A. Caballero, Nickel particles selectively confined in the mesoporous channels of SBA-15 yielding a very stable catalyst for DRM reaction, J. Phys. Chem. B 122 (2018) 500–510.

[52] D. Liu, X.Y. Quek, W.N.E. Cheo, R. Lau, A. Borgna, Y. Yang, MCM-41 supported nickel-based bimetallic catalysts with superior stability during carbon dioxide reforming of methane: Effect of strong metal–support interaction, J. Catal. 266 (2009) 380–390.

[53] L. Liu, Z. Yao, Y. Deng, F. Gao, B. Liu, L. Dong, Morphology and crystal-plane effects of nanoscale ceria on the activity of CuO/CeO2 for NO reduction by CO, ChemCatChem 3 (2011) 978–989.

[54] B.L. Newalkar, J. Olanrewaju, S. Komarneni, Microwave-hydrothermal synthesis and characterization of zirconium substituted SBA-15 mesoporous silica, J. Phys. Chem. B 105 (2001) 8356–8360.

[55] S.-Y. Chen, J.-F. Lee, S. Cheng, Pinacol-type rearrangement catalyzed by Zr-incorporated SBA-15, J. Catal. 270 (2010) 196–205.

[56] M. Araki, V. Ponec, Methanation of carbon monoxide on nickel and nickel-copper alloys, J. Catal. 44 (1976) 439–448.

[57] K. Chayakul, T. Srithanratana, S. Hengrasmee, Catalytic activities of Re–Ni/CeO2 bimetallic catalysts for water gas shift reaction, Catal. Today 175 (2011) 420–429.

[58] J.-H. Lin, P. Biswas, V.V. Guliants, S. Misture, Hydrogen production by water–gas shift reaction over bimetallic Cu–Ni catalysts supported on La-doped mesoporous ceria, Appl. Catal. A 387 (2010) 87–94.

[59] E.T. Saw, U. Oemar, M.L. Ang, H. Kus, S. Kawi, High-temperature water gas shift reaction on Ni–Cu/CeO2 catalysts: effect of ceria nanocrystal size on carboxylate formation, Catal. Sci. Technol. 6 (2016) 5336–5349.

[60] S. Ichikawa, H. Poppa, M. Boudart, Disproportionation of CO on small particles of silica-supported palladium, J. Catal. 91 (1985) 1–10.

[61] M. Agnelli, H.M. Swaan, C. Marquez-Alvarez, G.A. Martin, C. Mirodatos, CO Hydrogenation on a Nickel Catalyst: II. A Mechanistic Study by Transient Kinetics and Infrared Spectroscopy, J. Catal. 175 (1998) 117–128.

[62] A.A. Hakeem, R.S. Vásquez, J. Rajendran, M. Li, R.J. Berger, J.J. Delgado, F. Kapteijn, M. Makkee, The role of rhodium in the mechanism of the water–gas shift over zirconia supported iron oxide, J. Catal. 313 (2014) 34–45.

[63] H. Zhu, Z. Qin, W. Shan, W. Shen, J. Wang, Pd/CeO2–TiO2 catalyst for CO oxidation at low temperature: a TPR study with H2 and CO as reducing agents, J. Catal. 225 (2004) 267–277.

[64] A. Bueno-López, K. Krishna, M. Makkee, J.A. Moulijn, Enhanced soot oxidation by lattice oxygen via La3+-doped CeO2, J. Catal. 230 (2005) 237–248.

[65] M. Zhu, Ö. Yalçın, I.E. Wachs, Revealing structure-activity relationships in chromium free high temperature shift catalysts promoted by earth abundant elements, Appl. Catal. B 232 (2018) 205–212.

[66] Y. Zhai, D. Pierre, R. Si, W. Deng, P. Ferrin, A.U. Nilekar, G. Peng, J.A. Herron, D.C. Bell, H. Saltsburg, M. Mavrikakis, M. Flytzani-Stephanopoulos, Alkali-stabilized Pt-OHx species catalyze low-temperature water-gas shift reactions, Science 329 (2010) 1633.

[67] Z. Wu, M. Li, S.H. Overbury, On the structure dependence of CO oxidation over CeO2 nanocrystals with well-defined surface planes, J. Catal. 285 (2012) 61–73.

[68] T. Shido, Y. Iwasawa, Reactant-promoted reaction mechanism for water-gas shift reaction on Rh-doped CeO2, J. Catal. 141 (1993) 71–81.

[69] G. Jacobs, U.M. Graham, E. Chenu, P.M. Patterson, A. Dozier, B.H. Davis, Low-temperature water–gas shift: impact of Pt promoter loading on the partial reduction of ceria and consequences for catalyst design, J. Catal. 229 (2005) 499–512.

[70] L.C. Grabow, A.A. Gokhale, S.T. Evans, J.A. Dumesic, M. Mavrikakis, Mechanism of the water gas shift reaction on Pt: First principles, experiments, and microkinetic modeling, J. Phys. Chem. C 112 (2008) 4608–4617.

[71] A.A. Gokhale, J.A. Dumesic, M. Mavrikakis, On the mechanism of low-temperature water gas shift reaction on copper, J. Am. Chem. Soc. 130 (2008) 1402–1414.

[72] W.-J. Jang, J.-O. Shim, K.-W. Jeon, H.-S. Na, H.-M. Kim, Y.-L. Lee, H.-S. Roh, D.-W. Jeong, Design and scale-up of a Cr-free Fe-Al-Cu catalyst for hydrogen production from waste-derived synthesis gas, Appl. Catal. B 249 (2019) 72–81.

[73] D. Devaiah, P.G. Smirniotis, Effects of the Ce and Cr contents in Fe–Ce–Cr ferrite spinels on the high-temperature water–gas shift reaction, Ind. Eng. Chem. Res. 56 (2017) 1772–1781.

[74] M. Zhu, I.E. Wachs, Determining number of active sites and TOF for the high-temperature water gas shift reaction by iron oxide-based catalysts, ACS Catal. 6 (2016) 1764–1767.

[75] D. Damma, D. Jampaiah, A. Welton, P. Boolchand, A. Arvanitis, J. Dong, P.G. Smirniotis, Effect of Nb modification on the structural and catalytic property of Fe/Nb/M (M = Mn Co, Ni, and Cu) catalyst for high temperature water-gas shift reaction, Catal. Today (2019).

[76] X. Qi, M. Flytzani-Stephanopoulos, Activity and stability of Cu−CeO2 catalysts in high-temperature water−gas shift for fuel-cell applications, Ind. Eng. Chem. Res. 43 (2004) 3055–3062.

[77] Y. Cui, Z. Li, Z. Zhao, V.J. Cybulskis, K.D. Sabnis, C.W. Han, V. Ortalan, W.F. Schneider, J. Greeley, W.N. Delgass, F.H. Ribeiro, Participation of interfacial hydroxyl groups in the water-gas shift reaction over Au/MgO catalysts, Catal. Sci. Technol. 7 (2017) 5257–5266.

[78] J.H. Pazmiño, M. Shekhar, W. Damion Williams, M. Cem Akatay, J.T. Miller, W. Nicholas Delgass, F.H. Ribeiro, Metallic Pt as active sites for the water–gas shift reaction on alkali-promoted supported catalysts, J. Catal. 286 (2012) 279–286.

[79] A.A. Phatak, N. Koryabkina, S. Rai, J.L. Ratts, W. Ruettinger, R.J. Farrauto, G.E. Blau, W.N. Delgass, F.H. Ribeiro, Kinetics of the water–gas shift reaction on Pt catalysts supported on alumina and ceria, Catal. Today 123 (2007) 224–234.

[80] K.G. Azzam, I.V. Babich, K. Seshan, L. Lefferts, Role of Re in Pt–Re/TiO2 catalyst for water gas shift reaction: A mechanistic and kinetic study, Appl. Catal. B 80 (2008) 129–140.

[81] R.C. Catapan, A.A.M. Oliveira, Y. Chen, D.G. Vlachos, DFT Study of the water–gas shift reaction and coke formation on Ni(111) and Ni(211) surfaces, J. Phys. Chem. C 116 (2012) 20281–20291.

[82] M. Zhou, B. Liu, DFT Investigation on the competition of the water–gas shift reaction versus methanation on clean and potassium-modified nickel(1 1 1) surfaces, ChemCatChem 7 (2015) 3928–3935.

[83] K.-R. Hwang, C.-B. Lee, J.-S. Park, Advanced nickel metal catalyst for water–gas shift reaction, J. Power Sources 196 (2011) 1349–1352.

[84] S.H. Kim, J.H. Chung, Y.T. Kim, J. Han, S.P. Yoon, S.W. Nam, T.-H. Lim, H.-I. Lee, SiO2/Ni and CeO2/Ni catalysts for single-stage water gas shift reaction, Int. J. Hydrogen Energy 35 (2010) 3136–3140.

[85] Z.-J. Zhao, Z. Li, Y. Cui, H. Zhu, W.F. Schneider, W.N. Delgass, F. Ribeiro, J. Greeley, Importance of metal-oxide interfaces in heterogeneous catalysis: A combined DFT, microkinetic, and experimental study of water-gas shift on Au/MgO, J. Catal. 345 (2017) 157–169.

[86] R.R. Ford, Carbon monoxide adsorption on the transition metals, in: D.D. Eley, H. Pines, P.B. Weisz (Eds.), Adv. Catal., 1970, pp. 51–150.